ARTICLES
https://doi.org/10.1038/s41565-022-01153-w
nature nanotechnology

Check for updates

Ultra-low-energy programmable non-volatile silicon photonics based on phase-change materials with graphene heaters

Zhuoran Fang[1]✉, Rui Chen[1], Jiajiu Zheng[1], Asir Intisar Khan[2], Kathryn M. Neilson[2], Sarah J. Geiger[3], Dennis M. Callahan[3], Michael G. Moebius[3], Abhi Saxena[1], Michelle E. Chen[2,4], Carlos Rios[5,6], Juejun Hu[7], Eric Pop[2,4] and Arka Majumdar[1,8]✉

Silicon photonics is evolving from laboratory research to real-world applications with the potential to transform many technologies, including optical neural networks and quantum information processing. A key element for these applications is a reconfigurable switch operating at ultra-low programming energy—a challenging proposition for traditional thermo-optic or free carrier switches. Recent advances in non-volatile programmable silicon photonics based on phase-change materials (PCMs) provide an attractive solution to energy-efficient photonic switches with zero static power, but the programming energy density remains high (hundreds of attojoules per cubic nanometre). Here we demonstrate a non-volatile electrically reconfigurable silicon photonic platform leveraging a monolayer graphene heater with high energy efficiency and endurance. In particular, we show a broadband switch based on the technologically mature PCM $Ge_2Sb_2Te_5$ and a phase shifter employing the emerging low-loss PCM Sb_2Se_3. The graphene-assisted photonic switches exhibited an endurance of over 1,000 cycles and a programming energy density of $8.7 \pm 1.4\ aJ\ nm^{-3}$, that is, within an order of magnitude of the PCM thermodynamic switching energy limit ($\sim 1.2\ aJ\ nm^{-3}$) and at least a 20-fold reduction in switching energy compared with the state of the art. Our work shows that graphene is a reliable and energy-efficient heater compatible with dielectric platforms, including Si_3N_4, for technologically relevant non-volatile programmable silicon photonics.

In the past decade, programmable silicon photonic integrated circuits (PICs) have moved from traditional applications, such as optical interconnects[1] and signal processing[2], to emerging fields, such as optical neural networks[3], quantum information processing[4] and light detection and ranging[5]. All these applications require numerous optical components and switches. As PICs are scaled up, the physical size and energy consumption of individual photonic switches become increasingly critical. However, the traditional means of tuning silicon PICs, including thermo-optic[6] and free carrier dispersion effects[7], suffer from a large programming energy, large form factors, a volatile nature and a small change in the complex refractive index ($\Delta n < 0.01$). Recent progress in hybrid silicon photonics[8] could circumvent some of these limitations. For example, III–V/silicon modulators[9] based on the plasma dispersion and band-filling effects achieve a small half-wave voltage-length product ($V_\pi L$) of 0.047 V cm, silicon–lithium niobate modulators based on the Pockels effect afford low-energy (170 fJ) and ultra-fast (70 GHz) switching speed[10] and silicon–organic hybrid modulators operate at sub-femtojoule per bit[11]. Nevertheless, most approaches are still based on volatile field effects with limited complementary metal oxide semiconductor (CMOS) compatibility[9–11]. In contrast, non-volatile programming of PICs can greatly improve the energy efficiency because the static power consumption is zero, leading to true 'set-and-forget'-type switches[12]. In particular, chalcogenide-based phase-change materials (PCMs) can afford a feasible solution[13] as a result of a non-volatile microstructural phase transition[14], large contrast in complex refractive index[15] (typically $\Delta n \geq 1$) and CMOS compatibility[13]. In fact, PCMs have recently attracted considerable attention in the creation of programmable PICs with applications in, for example, photonic switches[16–19], photonic memory[20] and optical computing[21,22].

So far, the majority of the reported phase-change PICs have employed optical switching for reconfiguration[17,20,23]. In particular, high cyclability (>4,000)[24], strong optical phase modulation ($\sim 2\pi$) and low insertion loss (~0.5 dB) have been demonstrated by laser switching Sb_2Se_3 on silicon-on-insulator (SOI) waveguides[23]. Compared with optical switching, electrical switching provides a more attractive solution[13,25] for ease of scaling and the ability to switch a large volume of PCMs. Recent advances in electrically reconfigurable PCM-integrated PICs[16,18,26–29] have revealed that electrical switching by an external heater is a more effective approach than 'memory switching'[30,31], which is typically performed in electronic phase-change memory devices. 'Memory switching' switches only the volume that is necessary for conduction to change; hence, the optical contrast is very small (~0.6%)[32]. In contrast, switching by external heaters, such as forward-biased p-type/intrinsic/n-type (PIN) diodes[16], doped silicon[18,26] and indium tin oxide (ITO)[27–29], enables a larger volume of PCMs to undergo a phase transition, allowing high extinction ratio photonic switches. Despite the progress, fundamental challenges still

[1]Department of Electrical and Computer Engineering, University of Washington, Seattle, WA, USA. [2]Department of Electrical Engineering, Stanford University, Stanford, CA, USA. [3]The Charles Stark Draper Laboratory, Cambridge, MA, USA. [4]Department of Materials Science and Engineering, Stanford University, Stanford, CA, USA. [5]Department of Materials Science and Engineering, University of Maryland, College Park, MD, USA. [6]Institute for Research in Electronics and Applied Physics, University of Maryland, College Park, MD, USA. [7]Department of Materials Science and Engineering, Massachusetts Institute of Technology, Cambridge, MA, USA. [8]Department of Physics, University of Washington, Seattle, WA, USA. ✉e-mail: rogefzr@uw.edu; arka@uw.edu

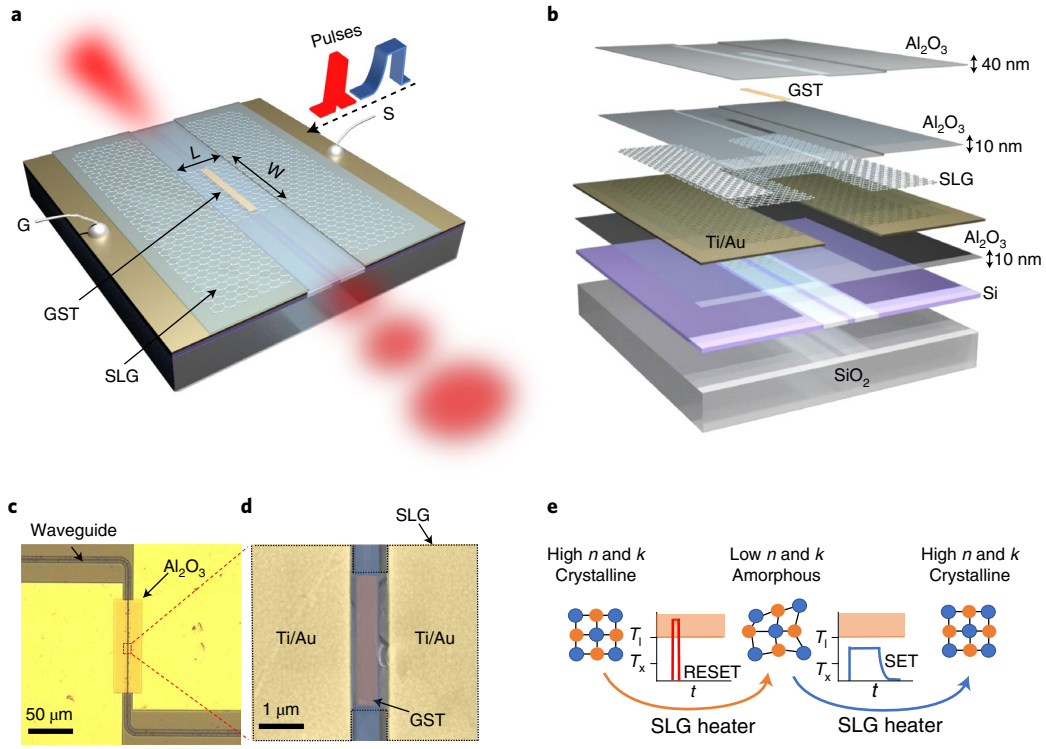

Fig. 1 | A graphene–PCM reconfigurable silicon photonic platform. a, Schematic of the device structure. SLG, single-layer graphene; S, signal electrode; G, ground electrode. **b**, The layered structure of the device. **c**, Optical micrograph of the waveguide switch. **d**, False-colour SEM image of the waveguide area, where the GST is patterned. The SLG area is indicated by the black dashed lines. **e**, Operating principle of the device. *k*, extinction coefficient; *t*, time.

exist for electrical switching using external heaters. First, the programming energy density remains high (hundreds of attojoules per cubic nanometre), far exceeding the theoretical limit[14] of ~1.2 aJ nm^{-3}. Second, the switching current and voltage typically reach tens of milliamperes and more than 5 V, considerably higher than the CMOS-driving currents and voltages (considering 5 V CMOS technologies[33]). Lastly, so far, no reliable transparent heaters have been reported that are compatible with dielectric platforms such as silicon nitride (Si_3N_4), a leading integrated photonic platform[34]. Polysilicon heaters have been used to thermally tune Si_3N_4 waveguides[35], but they are optically decoupled from the waveguides, leading to high power consumption (>100 mW) and slow response speed (~10 kHz). Transparent conducting oxides, such as ITO, have been investigated[27–29,36] for tuning PCMs on both Si and Si_3N_4 waveguides, but the reversible switching is still unsatisfactory. However, the switching of PCMs by graphene can provide outstanding performance[25], and the underlying physical mechanism was recently studied in a proof-of-principle device[37].

In this study, we leveraged these advances and state-of-the-art nanofabrication to design a highly optimized device that demonstrates the technological feasibility of non-volatile, electrically reconfigurable, hybrid PCM–silicon photonic platforms using a monolayer graphene heater. We first designed an ultra-compact broadband waveguide switch covering the whole telecommunication C-band based on absorption modulation using $Ge_2Sb_2Te_5$ (GST). The photonic switch was only 4.73 μm long and operated at a CMOS-driving current (≤2.78 mA) and voltage (≤5 V)[33]. Then, we employed the newly introduced low-loss PCM Sb_2Se_3 (ref. [24]) to demonstrate a graphene-assisted phase shifter using a micro-ring resonator that supports 14 distinct optical phase levels. The photonic switches showed ultra-low programming energy density (8.7 ± 1.4 aJ nm^{-3}) and high endurance (>1,000 cycles). Such high energy efficiency is possible because the atomically thin graphene, which exhibits high thermal conductivity and ultra-low heat capacity, considerably reduces the thermal mass needed to actuate the phase transition.

A graphene–PCM reconfigurable platform in silicon photonics

Our graphene–PCM hybrid switching platform consisted of a patterned graphene bridge across a planarized 220 nm SOI waveguide (Fig. 1a,b; for additional fabrication details, see Methods and Supplementary Fig. 1). The layered view in Fig. 1b shows that the PCM sits above the graphene, which is transferred onto the waveguides. The 40-nm-thick top Al_2O_3 layer encapsulates both the PCM and graphene to prevent oxidation and PCM reflowing during switching. There is an additional 10 nm atomic-layer-deposited (ALD) Al_2O_3 spacer between the graphene and the PCM that isolates the two materials. This spacer prevents the rupture of graphene due to the tension caused by the volume expansion and contraction of the PCM on switching. The metal contacts are placed only 300 nm away from the 500-nm-wide waveguide to reduce the graphene resistance while maintaining a low experimental metallic absorption loss of 0.002 ± 0.001 dB μm^{-1}. Such a low Ohmic loss, despite the proximity of the metals to the waveguides, is made possible by the geometry of the planarized waveguide (Supplementary Fig. 2a), which keeps the optical mode away from the metal plane and minimizes the evanescent interaction. The graphene has a large contact area (9.75 μm × 100 μm) with the metals to reduce the contact resistance, and it narrows at the bridge to restrict the current flow to the PCM region and to minimize absorptive loss from the graphene. The bridge region has a width *W* designed to be 200 nm longer than the length of the PCM and a length *L* fixed at 1.1 μm = (0.3 μm × 2) + 0.5 μm. An optical micrograph of the fabricated device is shown in Fig. 1c, and Fig. 1d shows the false-colour scanning electron microscopy (SEM) image of a 2.85 μm × 400 nm

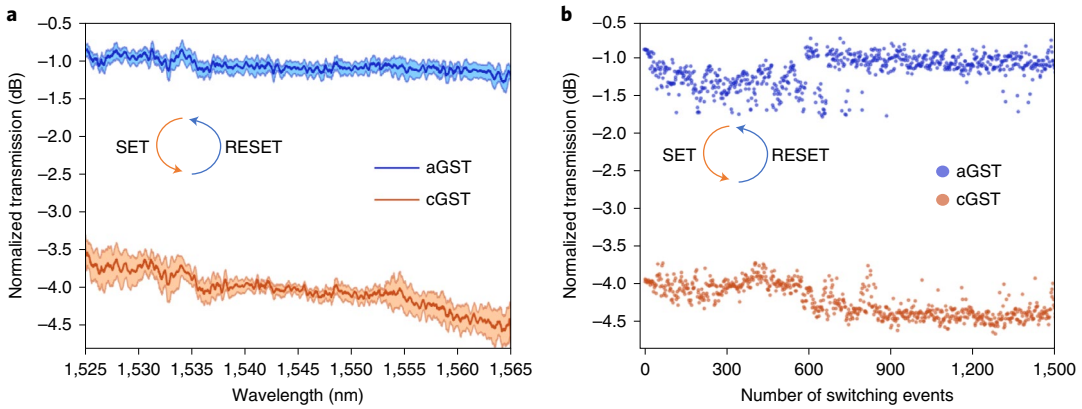

Fig. 2 | Graphene-assisted broadband waveguide switch based on GST. a, Reversible switching of GST on an SOI waveguide using a graphene heater. The switching conditions were 3 V, 100 µs pulse width and 120 µs trailing edge for SET, and 5 V, 400 ns pulse width and 8 ns trailing edge for RESET. Eight consecutive cycles were performed; the shaded area indicates the standard deviation of the cycles and the solid line indicates the average. The device spectrum is normalized to the spectrum of a bare waveguide. **b**, Cyclability of the switch for 1,500 switching events. The pulse conditions were the same as in **a**. Each pulse was temporally separated by 2 s to ensure long thermal relaxation. The transmission is normalized to the transmission of a bare waveguide. cGST, crystalline GST; aGST, amorphous GST.

GST patch on the waveguide, revealing the excellent accuracy of the lithographic alignment.

Figure 1e illustrates the operating principle of the graphene–PCM photonic switch. By applying a high amplitude and short voltage pulse, also known as a 'RESET' pulse, across the graphene bridge, the PCM is heated above its melting temperature T_l and rapidly quenched by removing the excitation. The melt–quench operation induces the amorphization of the PCM and transforms the PCM into a transparent and lower refractive index state. Application of a low amplitude and long voltage pulse, also known as a 'SET' pulse, across the graphene heater heats the PCM above its crystallization temperature T_x and below the melting point to return the PCM to its crystalline state. The long trailing edge ensures slow cooling of the material to complete the crystallization. The material is then restored to the higher absorption and refractive index crystalline state. The two devices discussed below leverage the absorption and refractive index modification of the PCM actuated by graphene heaters to realize a broadband on/off switch and a low-loss phase shifter, respectively.

Graphene-assisted broadband waveguide switch based on GST

We first explored a broadband waveguide switch based on the absorption modulation of GST. GST exhibited a large change in complex refractive index upon phase transition, giving rise to a remarkable modification of the optical mode of the GST-clad waveguide (Supplementary Fig. 2). Although the strong optical absorption of GST in the crystalline state makes it undesirable for phase-only control in the near infrared, the amplitude modulation of GST across a wide wavelength range is attractive for applications such as photonic memory[20] and optical computing[38]. Figure 2a shows the reversible switching of the waveguide spectrum between low (crystalline GST) and high (amorphous GST) transmission states for eight consecutive cycles using the device structure shown in Fig. 1c,d. The shaded regions of the spectra indicate the standard deviation for the eight switching cycles, clearly revealing excellent cycle-to-cycle reproducibility. A contrast of 3 dB in transmission can be observed across the entire telecommunication C-band with a 4.73-µm-long, 23-nm-thick GST. Temporal trace measurements (Supplementary Fig. 4a) confirmed that the change was non-volatile and hence caused by the GST. The 0.74 dB µm^{-1} optical contrast is slightly lower than that for GST placed directly on top of the waveguides[16] (in our device a 20 nm Al_2O_3 spacer is placed between the GST and waveguide), but agrees well with the optical mode simulations (Supplementary Fig. 2a). Heat transfer simulation also confirmed that the temperature reached the required threshold temperatures for both the crystallization and amorphization of GST (Supplementary Fig. 2b). The total switching energy for the amorphization was 5.55 nJ, corresponding to an energy density of 127.6 aJ nm^{-3}, and the energy dissipated by the graphene heater alone (that is, excluding the power loss at the contact resistance) was only 0.380 ± 0.062 nJ, equivalent to an energy density of 8.74 ± 1.42 aJ nm^{-3} (for details on estimating the graphene sheet resistance and switching power, see Supplementary Section 3). This represents a >20-fold reduction in the programming energy density compared with the state of the art[37] and within an order of magnitude of the ~1.2 aJ nm^{-3} fundamental limit[14]. Finally, we proved the high endurance of the device by performing 1,500 switching events on the graphene–GST photonic switch (Fig. 2b). An ~0.5 dB improvement in switching contrast was observed at around the 600th switching event (pulse conditions remain unchanged), which is likely attributable to a larger crystalline domain forming after the initial 'conditioning' steps[20]. It has previously been found that the initial pulsing of PCMs could give rise to ordered structures that act as seeds for subsequent crystal growth with minimal nucleation[39]. As a result, a larger volume of the PCM can be switched or 'activated'.

Graphene-assisted low-loss phase shifter based on Sb_2Se_3 in a micro-ring resonator

Phase shifters are frequently used in PICs to realize Mach–Zehnder modulators and 1×2 or 2×2 switches. The large optical absorption of GST in the crystalline state prohibits its use for phase-only modulation. In this study, we employed the recently reported[23,24] low-loss PCM Sb_2Se_3 to realize a graphene-assisted non-volatile phase shifter in a micro-ring resonator. We harnessed the transparent window of Sb_2Se_3 in the near infrared, where a negligible insertion loss of 0.002 ± 0.002 dB µm^{-1} of the Sb_2Se_3-loaded waveguide was extracted using a cut-back method at 1,550 nm (Supplementary Fig. 5). A schematic of the device is illustrated in Fig. 3a, an optical micrograph of the device is shown in Fig. 3b and a false-colour SEM image of a 6-µm-long, 400-nm-wide, 30-nm-thick Sb_2Se_3 patch on the waveguide is shown in Fig. 3c. Figure 3d shows the reversible tuning of a micro-ring resonance at 1,549 nm; the spectra of three

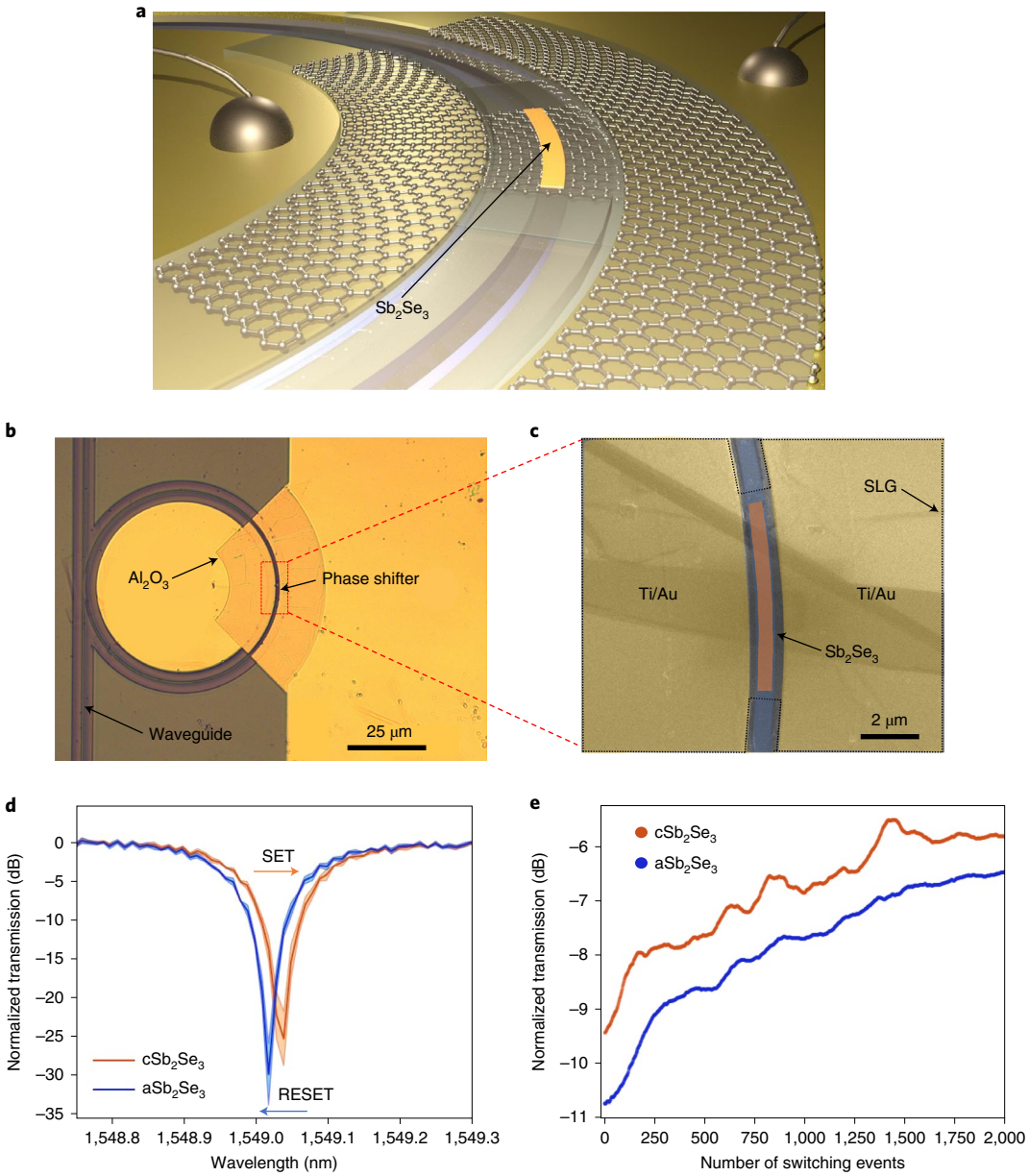

Fig. 3 | Graphene-assisted phase shifter based on Sb_2Se_3 in a micro-ring. a, Schematic of the graphene–Sb_2Se_3 phase shifter in a micro-ring. Note that an additional 10 nm sputtered SiO_2 layer is used to encapsulate the Sb_2Se_3. Such SiO_2 capping is not used for GST. **b**, Optical micrograph of the micro-ring resonator integrated with a phase shifter. **c**, False-colour SEM image of the micro-ring area, where the Sb_2Se_3 is patterned. The graphene area is indicated by the black dashed lines. **d**, Reversible switching of Sb_2Se_3 using a graphene heater on micro-rings. The switching conditions were 4 V, 100 μs pulse width and 120 μs trailing edge for SET, and 6.8 V, 400 ns pulse width and 8 ns trailing edge for RESET. Three consecutive cycles are plotted; the shaded areas indicate the standard deviation of the cycles and the solid lines indicate the average. The spectra are normalized to the spectrum of a bare waveguide. **e**, Cyclability of the switch for 2,000 switching events. The switching conditions were 4 V, 100 μs pulse width and 120 μs trailing edge for SET, and 6.4 V, 400 ns pulse width and 8 ns trailing edge for RESET. Each pulse was temporally separated by 2 s to ensure long thermal relaxation. The transmission is normalized to the transmission of a bare waveguide. The data have been filtered by a 50-point moving average to reduce the fluctuation caused by thermal noise.

cycles are plotted and the shaded regions indicate the standard deviations of the cycles.

The total switching energy for amorphization was 9.25 nJ (128.4 aJ nm^{-3}) and the energy dissipated by the graphene heater alone (that is, excluding the power loss at the contact resistance) was only 0.57 ± 0.09 nJ and 7.9 ± 1.3 aJ nm^{-3} (for details on estimating the graphene sheet resistance and switching power, see Supplementary Section 3). A maximum resonance shift of 0.021 nm was extracted, which corresponds to a phase shift of 0.00822π and $V_\pi L$ of 0.496 V cm (assuming a switching voltage of 6.8 V), representing a threefold improvement compared with the state-of-the-art silicon p-type/n-type (PN) phase shifter[40]. The phase shift matches the simulation (Supplementary Fig. 2), but is smaller than the recently reported value[18] due to the intrinsic smaller index change in our Sb_2Se_3 and the use of the 20 nm Al_2O_3 spacer. We believe that the phase modulation can be further improved with higher quality Sb_2Se_3 and a thinner spacer. The increase in the insertion loss (IL) of Sb_2Se_3 in the crystalline state was extracted by fitting the Q factor of the resonances and was estimated to be 0.006 ± 0.002 dB μm^{-1}. The IL of the metal and graphene was estimated to be 0.002 ± 0.001 dB μm^{-1}

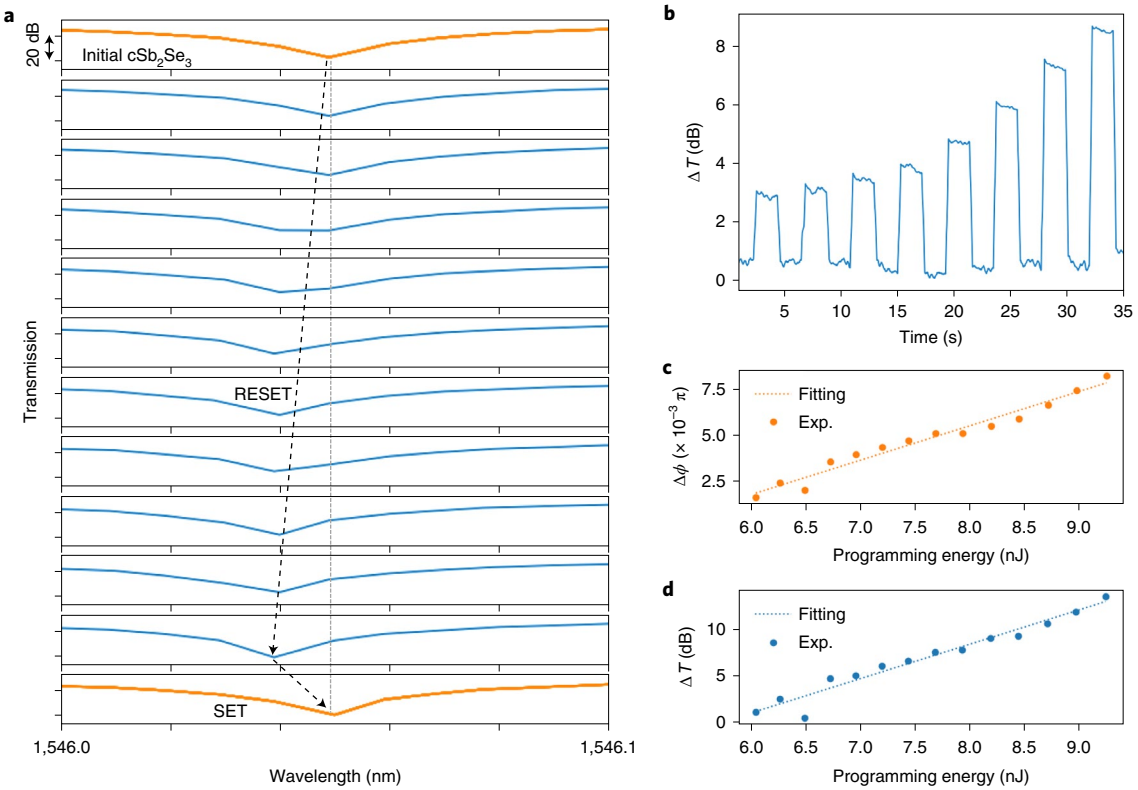

Fig. 4 | Quasi-continuous phase modulation using the graphene–Sb_2Se_3 phase shifter. a, Quasi-continuous tuning of micro-ring resonance by step amorphization. The SET conditions were 4 V, 100 µs pulse width and 120 µs trailing edge. For RESET, the amplitude was increased monotonically from 5.5 V to 6.4 V, and the pulse width and trailing edge were fixed at 400 ns and 8 ns, respectively. **b**, Temporal trace of a continuous programming iteration with a monotonically increasing RESET pulse amplitude from 5.5 V to 6.9 V followed by a SET pulse. Eight transmission levels are clearly resolved. The pulse width and trailing edge of the RESET pulse were fixed at 400 ns and 8 ns, respectively. The SET conditions were the same as in **a**. **c**, Change in phase shift ($\Delta\phi$) with programming energy. Fourteen phase levels can be resolved, with the phase shift increasing linearly with programming energy. Exp., experimental. **d**, Change in transmission caused by the variation in the phase shift with programming energy. Fourteen transmission levels can be resolved. The transmission contrast increases linearly with the programming energy, matching very well with **c**.

and $0.047 \pm 0.006\,dB\,\mu m^{-1}$, respectively, from fitting the micro-ring spectra after each overlay step. The total IL was only ~0.33 dB for a device with a length of 6 µm. The graphene IL is slightly lower than the loss measured in a similar graphene-on-micro-ring structure[41], for which an IL of ~$0.07\,dB\,\mu m^{-1}$ was extracted. The reduction in the graphene IL in our work is likely attributable to a lower carrier density and the 10 nm ALD Al_2O_3 spacer between the graphene and the waveguides, compared with the 3-nm-thick hexagonal boron nitride used in previous work[41]. Optical losses in graphene can be further suppressed by electrical gating to the Pauli blocking region[42,43].

Lastly, we demonstrated excellent endurance of the device by performing 2,000 switching events on the phase shifter (Fig. 3e). The laser wavelength was slightly detuned from the resonance wavelength to mitigate transmission fluctuations from the thermal drift (Methods). The gradual increase in transmission observed with cycling time was caused by the temperature-induced drift of the resonance wavelength away from the initial laser wavelength. Comparison of the spectrum of the as-fabricated micro-ring with that measured after 1,100 continuous cycles (Supplementary Fig. 6) showed that there was no broadening of the resonance peak, implying that the cycling did not induce any damage in the device. The temporal trace recorded after 1,100 cycles (Supplementary Fig. 4b) still showed a large optical contrast of 7 dB, as the laser wavelength was parked near the resonance. Transmission measurements taken between the switching events (duration of 2 s) indicated that the change was non-volatile and was indeed caused by Sb_2Se_3. The transient response of the switching was characterized using a 150 MHz fast photoreceiver (Supplementary Fig. 9). Next, we compared our graphene–PCM hybrid platform with other electrical switching approaches in PCM-based photonics. Supplementary Fig. 10 clearly shows that our graphene–PCM switch not only exhibits one of the highest endurances (>1,000 cycles), but also produces the lowest switching energy density ($8.7 \pm 1.4\,aJ\,nm^{-3}$) reported so far. Finally, we compared our electrical switching study with previously reported optical switching data (Supplementary Table 2 in Supplementary Section 11).

Quasi-continuous multilevel phase modulation using the graphene–Sb_2Se_3 phase shifter

It is well known that PCMs can support multilevel operation, and this property is widely exploited in electronic memory[31], photonic memory[44] and most recently in optical neural networks[22]. After realizing bistable switching, we further found that the phase shifter can be tuned quasi-continuously to attain multiple optical phase levels by controlling the programming energy. Figure 4a shows that as the programming voltage was monotonically increased in steps of 0.1 V from 5.5 V to 6.4 V (the pulse width and trailing edge were fixed at 400 ns and 8 ns, respectively), the resonance dip shifted gradually to a shorter wavelength, with the intermediate states corresponding to partially amorphous PCMs. This effect was caused by an increasingly larger hotspot in the centre of the heater, resulting in an increasingly larger area of the PCM being amorphized. As a result, the resonance dip shifted gradually to a shorter wave-

length, with these intermediate states corresponding to partially amorphous PCMs. After ten pulses of increasing amplitude, a SET pulse of 4 V (100 µs pulse width and 120 µs trailing edge) was used to return the resonance to the original position. The resonance wavelength of the SET state perfectly matched the resonance wavelength of the initial crystalline state, as indicated by the grey dashed line in Fig. 4a. The time dynamic response was investigated by increasing the programming voltage in increments of 0.2 V from 5.5 V to 6.9 V, and the transmission was continuously monitored with respect to time, as shown in Fig. 4b. After each RESET operation, the PCM returned to the initial crystalline state using the same SET pulse of 4 V. Eight distinct transmission levels could be clearly resolved with ~1 dB contrast between adjacent levels. To better quantify the multilevel phase modulation, we extracted the phase shift from the change in the resonance wavelength from each RESET pulse and plotted the phase shift against the programming energy (Fig. 4c). Fourteen phase levels were attained by increasing the programming energy from 6 nJ to 9.5 nJ, with the phase increasing linearly with the programming energy. Figure 4d shows that the resulting change in transmission from the phase modulation matches very well with Fig. 4c. The reproducibility of the multilevel operation was evaluated for five iterations (Supplementary Fig. 11b) and showed that although the transmission levels were not entirely deterministic, the mean transmission increased with the programming energy almost linearly. Similarly, multilevel operations could also be realized in the graphene–GST waveguide switch, for which seven distinct transmission levels were obtained (Supplementary Fig. 11a). We point out that, although not demonstrated in the current work, multilevel operation attained by step crystallization is also possible by adjusting the pulse amplitude and width, as shown by others[20,28,31].

Conclusion

We have reported two examples of non-volatile, electrically switchable, silicon photonic platforms leveraging a monolayer graphene heater: a GST-based broadband waveguide switch and a Sb_2Se_3-clad phase shifter. We achieved an ultra-low programming energy density (8.7 ± 1.4 aJ nm^{-3}) and high endurance (>1,000 cycles) at CMOS-driving voltage (≤5 V) and current (≤2.78 mA). Our results prove that graphene is not only a reliable heater that can be controlled by CMOS electronics, but also compatible with dielectric platforms, including Si_3N_4, and can potentially be used on arbitrary substrates. We believe that further advances and optimization can come from the following sources: reducing the insertion loss of graphene by electrical gating to the Pauli blocking region[42,43], reducing the graphene contact resistance and contact area using one-dimensional edge contacts[45] and improving the phase modulation of the Sb_2Se_3 phase shifter using higher quality Sb_2Se_3[18,23] and a thinner Al_2O_3 spacer. Additionally, graphene transfer is not yet available in commercial CMOS foundries, although wafer-scale synthesis, transfer and integration with photonic devices have been reported[46,47]. Wafer-scale graphene transfer can be fully automated and it is the only step that needs to be added between the planarization of silicon waveguides and metallization in a standard CMOS process[48]. Recent reports on graphene-based silicon photonic devices[41,43] have described remarkable performance, superior to their counterparts in monolithic platforms, making full integration of wafer-scale graphene transfer with the current foundry processes highly attractive. We also note that graphene transfer and patterning processes happen at relatively low temperature and do not affect the underlying silicon photonic platform.

Online content

Any methods, additional references, Nature Research reporting summaries, source data, extended data, supplementary information, acknowledgements, peer review information; details of author contributions and competing interests; and statements of data and code availability are available at https://doi.org/10.1038/s41565-022-01153-w.

Received: 17 December 2021; Accepted: 13 May 2022;
Published online: 4 July 2022

References

1. Cheng, Q., Bahadori, M., Glick, M., Rumley, S. & Bergman, K. Recent advances in optical technologies for data centers: a review. *Optica* **5**, 1354–1370 (2018).
2. Pérez, D. et al. Multipurpose silicon photonics signal processor core. *Nat. Commun.* **8**, 636 (2017).
3. Shen, Y. et al. Deep learning with coherent nanophotonic circuits. *Nat. Photon.* **11**, 441–446 (2017).
4. Arrazola, J. M. et al. Quantum circuits with many photons on a programmable nanophotonic chip. *Nature* **591**, 54–60 (2021).
5. Rogers, C. et al. A universal 3D imaging sensor on a silicon photonics platform. *Nature* **590**, 256–261 (2021).
6. Watts, M. R. et al. Adiabatic thermo-optic Mach–Zehnder switch. *Opt. Lett.* **38**, 733–735 (2013).
7. Thomson, D. J. et al. 50-Gb/s silicon optical modulator. IEEE Photon. *Technol. Lett.* **24**, 234–236 (2012).
8. Bogaerts, W. et al. Programmable photonic circuits. *Nature* **586**, 207–216 (2020).
9. Han, J.-H. et al. Efficient low-loss InGaAsP/Si hybrid MOS optical modulator. *Nat. Photon.* **11**, 486–490 (2017).
10. He, M. et al. High-performance hybrid silicon and lithium niobate Mach–Zehnder modulators for 100 Gbit s^{-1} and beyond. *Nat. Photon.* **13**, 359–364 (2019).
11. Koeber, S. et al. Femtojoule electro-optic modulation using a silicon–organic hybrid device. *Light Sci. Appl.* **4**, e255 (2015).
12. Rudolph, T. Why I am optimistic about the silicon-photonic route to quantum computing. *APL Photon.* **2**, 030901 (2017).
13. Fang, Z., Chen, R., Zheng, J. & Majumdar, A. Non-volatile reconfigurable silicon photonics based on phase-change materials. *IEEE J. Sel. Top. Quantum Electron.* https://doi.org/10.1109/JSTQE.2021.3120713 (2021).
14. Raoux, S., Xiong, F., Wuttig, M. & Pop, E. Phase change materials and phase change memory. *MRS Bull.* **39**, 703–710 (2014).
15. Shportko, K. et al. Resonant bonding in crystalline phase-change materials. *Nat. Mater.* **7**, 653–658 (2008).
16. Zheng, J. et al. Nonvolatile electrically reconfigurable integrated photonic switch enabled by a silicon PIN diode heater. *Adv. Mater.* **32**, 2001218 (2020).
17. Zheng, J. et al. GST-on-silicon hybrid nanophotonic integrated circuits: a non-volatile quasi-continuously reprogrammable platform. *Opt. Mater. Express* **8**, 1551–1561 (2018).
18. Ríos, C. et al. Ultra-compact nonvolatile photonics based on electrically reprogrammable transparent phase change materials. Preprint at https://arxiv.org/abs/2105.06010 (2021).
19. Xu, P., Zheng, J., Doylend, J. K. & Majumdar, A. Low-loss and broadband nonvolatile phase-change directional coupler switches. *ACS Photon.* **6**, 553–557 (2019).
20. Ríos, C. et al. Integrated all-photonic non-volatile multi-level memory. *Nat. Photon.* **9**, 725–732 (2015).
21. Feldmann, J. et al. Calculating with light using a chip-scale all-optical abacus. *Nat. Commun.* **8**, 1256 (2017).
22. Feldmann, J. et al. Parallel convolutional processing using an integrated photonic tensor core. *Nature* **589**, 52–58 (2021).
23. Delaney, M. et al. Nonvolatile programmable silicon photonics using an ultralow-loss Sb_2Se_3 phase change material. *Sci. Adv.* **7**, eabg3500 (2021).
24. Delaney, M., Zeimpekis, I., Lawson, D., Hewak, D. W. & Muskens, O. L. A new family of ultralow loss reversible phase-change materials for photonic integrated circuits: Sb_2S_3 and Sb_2Se_3. *Adv. Funct. Mater.* **30**, 2002447 (2020).
25. Zheng, J., Zhu, S., Xu, P., Dunham, S. & Majumdar, A. Modeling electrical switching of nonvolatile phase-change integrated nanophotonic structures with graphene heaters. *ACS Appl. Mater. Interfaces* **12**, 21827–21836 (2020).
26. Zhang, H. et al. Miniature multilevel optical memristive switch using phase change material. *ACS Photon.* **6**, 2205–2212 (2019).
27. Kato, K., Kuwahara, M., Kawashima, H., Tsuruoka, T. & Tsuda, H. Current-driven phase-change optical gate switch using indium–tin-oxide heater. *Appl. Phys. Express* **10**, 072201 (2017).
28. Taghinejad, H. et al. ITO-based microheaters for reversible multi-stage switching of phase-change materials: towards miniaturized beyond-binary reconfigurable integrated photonics. *Opt. Express* **29**, 20449–20462 (2021).
29. Fang, Z. et al. Non-volatile reconfigurable integrated photonics enabled by broadband low-loss phase change material. *Adv. Opt. Mater.* **9**, 2002049 (2021).
30. Xiong, F., Liao, A. D., Estrada, D. & Pop, E. Low-power switching of phase-change materials with carbon nanotube electrodes. *Science* **332**, 568–570 (2011).

31. Khan, A. I. et al. Ultralow-switching current density multilevel phase-change memory on a flexible substrate. *Science* **373**, 1243–1247 (2021).
32. Farmakidis, N. et al. Plasmonic nanogap enhanced phase-change devices with dual electrical-optical functionality. *Sci. Adv.* **5**, eaaw2687 (2019).
33. Ballan, H. & Declercq, M. *High Voltage Devices and Circuits in Standard CMOS Technologies* (Springer, 2013).
34. Moss, D. J., Morandotti, R., Gaeta, A. L. & Lipson, M. New CMOS-compatible platforms based on silicon nitride and Hydex for nonlinear optics. *Nat. Photon.* **7**, 597–607 (2013).
35. Heimala, P., Katila, P., Aarnio, J. & Heinamaki, A. Thermally tunable integrated optical ring resonator with poly-Si thermistor. *J. Lightwave Technol.* **14**, 2260–2267 (1996).
36. Fang, Z., Zheng, J., & Majumdar, A. Non-volatile integrated photonics enabled by broadband transparent phase change material. In *Conference on Lasers and Electro-Optics* JTh2B.3 (Optical Society of America, 2020); https://doi.org/10.1364/CLEO_AT.2020.JTh2B.3
37. Ríos, C. et al. Multi-level electro-thermal switching of optical phase-change materials using graphene. *Adv. Photon. Res.* **2**, 2000034 (2021).
38. Ríos, C. et al. In-memory computing on a photonic platform. *Sci. Adv.* **5**, eaau5759 (2019).
39. Loke, D. K. et al. Ultrafast nanoscale phase-change memory enabled by single-pulse conditioning. *ACS Appl. Mater. Interfaces* **10**, 41855–41860 (2018).
40. Xiong, C. et al. Monolithic 56 Gb/s silicon photonic pulse-amplitude modulation transmitter. *Optica* **3**, 1060–1065 (2016).
41. Schuler, S. et al. High-responsivity graphene photodetectors integrated on silicon microring resonators. *Nat. Commun.* **12**, 3733 (2021).
42. Wang, F. et al. Gate-variable optical transitions in graphene. *Science* **320**, 206–209 (2008).
43. Sorianello, V. et al. Graphene–silicon phase modulators with gigahertz bandwidth. *Nat. Photon.* **12**, 40–44 (2018).
44. Li, X. et al. Fast and reliable storage using a 5 bit, nonvolatile photonic memory cell. *Optica* **6**, 1–6 (2019).
45. Wang, L. et al. One-dimensional electrical contact to a two-dimensional material. *Science* **342**, 614–617 (2013).
46. Gao, L. et al. Face-to-face transfer of wafer-scale graphene films. *Nature* **505**, 190–194 (2014).
47. Lee, Y. et al. Wafer-scale synthesis and transfer of graphene films. *Nano Lett.* **10**, 490–493 (2010).
48. Romagnoli, M. et al. Graphene-based integrated photonics for next-generation datacom and telecom. *Nat. Rev. Mater.* **3**, 392–414 (2018).

Methods

Device fabrication. The graphene–PCM photonic switch was fabricated on a 220-nm-thick silicon layer on top of a 3-μm-thick buried oxide layer (SOITECH). Supplementary Fig. 1 shows the schematics of fabrication flow. The pattern was defined by a JEOL JBX-6300FS 100 kV electron-beam lithography (EBL) system using a positive tone ZEP-520A resist. The 220 nm fully etched ridge waveguides were prepared by inductively coupled plasma reactive ion etching (ICP-RIE) in fluorine-based gases. Before removing the resists, 220 nm SiO_2 was evaporated onto the resist-coated waveguides by electron-beam evaporation. The lift-off of SiO_2 was completed by sonication in methylene chloride for 3 min, which led to planarized waveguides. Then, 10 nm thermal ALD Al_2O_3 (H_2O precursor at 150 °C) was grown on the substrate to prevent the formation of a semiconductor and metal junction between the graphene and silicon. A second EBL step using a positive tone poly(methyl methacrylate) (PMMA) resist was subsequently carried out to create windows for the deposition of Ti/Au. After development, 5 nm Ti followed by 100 nm Au were deposited onto the chip by electron-beam evaporation. The Ti/Au was lifted off by immersing the chip in methylene chloride. Monolayer graphene (Graphenea) grown by chemical vapour deposition was transferred onto the chip by the standard PMMA wet transfer technique[49] and then patterned by EBL using a maN 2403 negative resist. Then, O_2 plasma was used to etch away the graphene that was not protected by the resist, followed by deposition of another 10 nm thermal ALD Al_2O_3 capping layer to protect the graphene during the subsequent fabrication steps. The high quality of the transferred graphene in the fabricated devices was confirmed by Raman spectroscopy (Supplementary Fig. 8). A fourth EBL overlay step was conducted to expose the PMMA resist before depositing GST or Sb_2Se_3 by magnetron sputtering. Then, 23 nm GST was deposited by magnetron sputtering (Lesker Lab 18) using a GST target at 28 W d.c. power and a base pressure of $\sim 5 \times 10^{-7}$ torr. The Ar flow rate was controlled to maintain a sputtering pressure of 3.5 mtorr. Sb_2Se_3 was deposited using a magnetron sputtering system at 30 W radiofrequency (RF) power under a deposition pressure of 4 mtorr and an Ar flow of 30 $cm^3 min^{-1}$. The deposition rate for Sb_2Se_3 was ~1 nm min^{-1}. Additionally, the samples were capped with 10 nm SiO_2 sputtered in situ (150 W RF power, 4 mtorr pressure and an Ar flow of 30 $cm^3 min^{-1}$) to prevent oxidation during sample shipping. For the selenide deposition, the sputtering chamber was subjected to several pre-deposition and post-deposition treatments, including cleaning the chamber followed by annealing and cleaning with O_2 plasma. Prior to Sb_2Se_3 deposition, the sputtering chamber was baked at 400 °C for 6 h (under vacuum), followed by cooling to room temperature to drive out gases and other contaminants. The toxic residual hydrogen selenide formed during Sb_2Se_3 deposition was removed by flowing O_2 plasma for 1 h prior to opening the sputtering chamber. The atomic ratio of Sb_2Se_3 after deposition was confirmed by X-ray photoelectron spectroscopy to be Sb/Se ≈ 44:56, which is close to the sputtering target stoichiometry of Sb/Se ≈ 40:60. Immediately after lifting off the PCM in methylene chloride, a 40 nm ALD Al_2O_3 layer was grown on the chip to protect the PCM from oxidation and reflowing during switching. To allow good electrical contact between the probes and the metal pads, a fifth EBL step was performed to open windows in the PMMA resist at the contact regions for Al_2O_3 etching. The Al_2O_3 on top of the contacts was etched away by ICP-RIE in chlorine-based gases. Finally, the PCMs were initialized into the fully crystalline state by rapid thermal annealing at 200 °C for 10 min under N_2 atmosphere before measurement. The patterned graphene did not peel off after subsequent fabrication steps owing to its protection by 10 nm ALD alumina.

Experimental set-up and measurements. The waveguides and micro-rings were characterized using a vertical fibre-coupling set-up[16]. All the measurements were performed under ambient conditions, with the temperature of the stage fixed at ~26 °C by a thermoelectric controller (TE Technology, TC-720) to prohibit a serious thermal shift of the resonators. The input light was provided by a tunable continuous-wave laser (Santec, TSL-510) and its polarization was controlled by a manual fibre polarization controller (Thorlabs, FPC526) to match the fundamental quasi-transverse-electric mode of the waveguides.

A low-noise power meter (Keysight, 81634B) was used to collect the static optical output from the grating couplers. Transmission spectra were recorded after the fabrication of bare micro-rings, deposition of the metal, transfer of the SLG and deposition of Sb_2Se_3 to determine the change in optical losses in each step. In the electrical characterization, electrical signals were applied to the metal contacts through a pair of d.c. probes controlled by two probe positioners (Cascade Microtech, DPP105-M-AI-S). The voltage sweep and current measurements were conducted using a source meter (Keithley, 2450). The generated current–voltage (I–V) curves were used to estimate the power of the applied pulses. The SET and RESET pulses were generated by a pulse function arbitrary generator (Keysight, 81150A). To reconfigure the graphene–GST photonic switch, we used a 5 V voltage pulse (2.78 mA), 400 ns pulse width and 8 ns rising/trailing edge to induce amorphization. For crystallization, a 3 V voltage pulse (1.79 mA), 100 μs pulse width and 120 μs trailing edge were used. To reconfigure the graphene–Sb_2Se_3 phase shifter, we used a 6.8 V voltage pulse (3.4 mA), 400 ns pulse width and 8 ns rising/trailing edge to induce amorphization. For crystallization, a 4 V voltage pulse (2.0 mA), 100 μs pulse width and 120 μs trailing edge were used. The voltage was the actual voltage applied across the device as the impedance was matched by setting the load impedance of the function generator to the total resistance of the device determined from the I–V curve. The graphene could withstand a maximum current typically of around 3 mA in our experiments. To perform the endurance test shown in Fig. 3e, the laser wavelength was initially parked near the resonance, which gives a larger optical contrast, but later drifts away from the resonance, leading to a simultaneous increase in transmission in both states and a slightly decreased contrast. The data were filtered by a 50-point moving average to reduce the fluctuation caused by thermal noise. The resonance drift of high-Q resonators due to temperature variation in the surroundings is not an uncommon issue due to the relatively strong thermo-optic effect of silicon, and integrated metallic heaters near the resonators are normally used to stabilize the temperature[50,51]. Optimized thermal stabilization is beyond the scope of this paper and will be explored in future work. To measure the transient response of the switch (Supplementary Fig. 9), the output light from the grating couplers was amplified using an optical fibre amplifier (Amonics, AEDFA-30-B-FA), and the amplified signal was detected with a 150 MHz near-infrared fast photoreceiver (Thorlabs, PDB450C) connected to an oscilloscope.

Data availability

The data that support the findings of this study are available from the corresponding authors upon reasonable request.

References

49. Liang, X. et al. Toward clean and crackless transfer of graphene. *ACS Nano* **5**, 9144–9153 (2011).
50. Atabaki, A. H. et al. Integrating photonics with silicon nanoelectronics for the next generation of systems on a chip. *Nature* **556**, 349–354 (2018).
51. Sun, C. et al. Single-chip microprocessor that communicates directly using light. *Nature* **528**, 534–538 (2015).

Acknowledgements

This research was funded by the National Science Foundation (NSF-1640986 and NSF-2003509), an ONR-YIP Award, a DARPA-YFA Award, the Draper Laboratory and Intel. Part of this work was conducted at the Washington Nanofabrication Facility/Molecular Analysis Facility, a National Nanotechnology Coordinated Infrastructure (NNCI) site at the University of Washington with partial support from the National Science Foundation (NNCI-1542101 and NNCI-2025489). We thank S. Moazeni for allowing us to use the high-speed photoreceiver at the University of Washington.

Author contributions

Z.F. and A.M. conceived the project. Z.F. simulated, designed and fabricated the devices. Z.F. led the switching experiments, optical characterizations and performed the data analysis. R.C. helped with the experiments and characterizations. J.Z. developed the initial fabrication process flow and design of the experiments. J.Z. and R.C. helped with the data analysis. A.I.K. and K.M.N. deposited the Sb_2Se_3 materials. A.S. illustrated the device schematics. M.E.C. advised on the SLG transfer process. C.R. and J.H. advised on the device design and fabrication process. E.P. facilitated the Sb_2Se_3 deposition and advised on the transfer of SLG. A.M., S.J.G., D.M.C. and M.G.M. supervised the overall progress of the project. Z.F. wrote the manuscript with input from all the authors.

Competing interests

All authors are listed as co-inventors on a US patent provisional application (patent application number 63/365,135) on the ultra-low-energy phase shifter filed by the Charles Stark Draper Laboratory.

Additional information

Supplementary information The online version contains supplementary material available at https://doi.org/10.1038/s41565-022-01153-w.

Correspondence and requests for materials should be addressed to Zhuoran Fang or Arka Majumdar.

Peer review information *Nature Nanotechnology* thanks Otto Muskens and Linjie Zhou for their contribution to the peer review of this work.

nature portfolio

https://doi.org/10.1038/s41565-022-01153-w

Supplementary information

Ultra-low-energy programmable non-volatile silicon photonics based on phase-change materials with graphene heaters

In the format provided by the authors and unedited

Supplementary information
Ultra-low energy programmable nonvolatile silicon photonics based on phase change materials with graphene heaters

Zhuoran Fang[1,*], Rui Chen[1], Jiajiu Zheng[1], Asir Intisar Khan[3], Kathryn M. Neilson[3], Sarah J. Geiger[5], Dennis M. Callahan[5], Michael G. Moebius[5], Abhi Saxena[1], Michelle E. Chen[3,4], Carlos Rios[6,7], Juejun Hu[8], Eric Pop[3,4], Arka Majumdar[1,2,*]

[1]*Department of Electrical and Computer Engineering, University of Washington, Seattle, WA 98195, USA*
[2]*Department of Physics, University of Washington, Seattle, WA 98195, USA*
[3]*Department of Electrical Engineering, Stanford University, Stanford, CA 94305, USA*
[4]*Department of Materials Science and Engineering, Stanford University, Stanford, CA 94305, USA*
[5]*The Charles Stark Draper Laboratory, Cambridge, MA 02139, USA*
[6]*Department of Materials Science and Engineering, University of Maryland, College Park, MD 20742, USA*
[7]*Institute for Research in Electronics & Applied Physics, University of Maryland, College Park, MD 20742, USA*
[8]*Department of Materials Science and Engineering, Massachusetts Institute of Technology, MA 02139, USA*

**Email: rogefzr@uw.edu and arka@uw.edu*

The Supplementary Information includes:

S1. Fabrication flow of single-layer graphene (SLG)-phase change material (PCM) reconfigurable silicon photonic platform

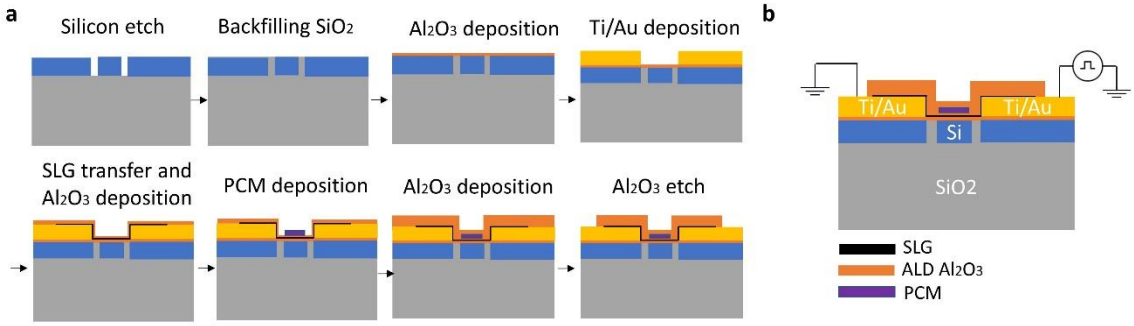

Figure S1: Fabrication flow schematics of SLG-PCM reconfigurable silicon photonic platform. a Fabrication process flow of the SLG-PCM photonic switch. **b** The cross-section of the final fabricated device.

S2. Optical mode and heat transfer simulations

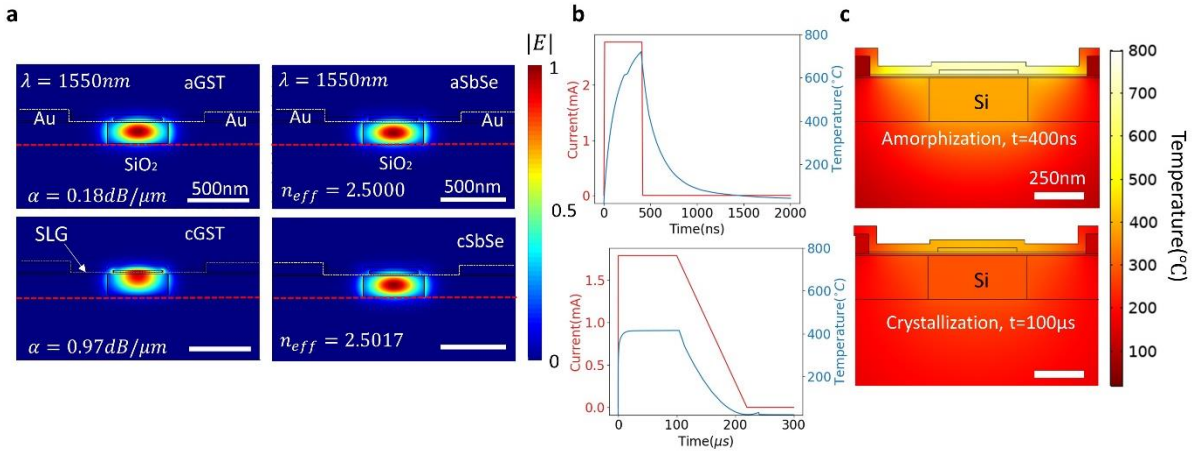

Figure S2: Optical mode and heat transfer simulations of the SLG-PCM photonic switch. a Simulated fundamental TE mode profiles of 23nm GST (left panel) and 30nm Sb_2Se_3 (right panel) on planarized SOI waveguides at 1550nm. The optical constants of GST and Sb_2Se_3 at 1550nm are extracted from cutback measurements using microring resonators. The white dashed lines indicate the presence of SLG in the simulation. The red dashed lines indicate the boundaries between the device layer (220nm Si) and the buried oxide. **b** Simulated temperature variation with time under the measured current for amorphization (top) and crystallization (bottom). The red curves indicate the injecting current while the blue curves indicate the temperature of GST. **c** Simulated temperature distribution at 400ns under injecting current of 2.78mA (top) and at 100μs under current of 1.89mA (bottom).

Here, we present the optical and heat transfer simulation results which are compared to the experimental results. The mode simulation is performed using Lumerical Mode solutions while the heat transfer simulation is performed using COMSOL Multiphysics heat transfer and electric current modules. Fig. S2a left panel shows that the fundamental quasi-transverse electric (TE) mode at 1550nm is confined in the SLG-GST cladded planarized waveguide and there is a large optical attenuation change $\Delta\alpha = 0.79\ dB/\mu m$ due to the phase transition of 23nm GST. This matches well with our experiments where we extract an attenuation change of $0.74\ dB/\mu m$ and confirms that we have fully changed the entire volume of GST. The small discrepancy is due to the batch-to-batch fabrication variations in deposited material thickness, dimensions, and etched waveguide dimensions. The change in extinction coefficients of GST

in amorphous and crystalline states on silicon waveguides is extracted from a cutback measurements using microrings as discussed in our previous works[1–3]. The optical constants extracted from ellipsometry measurements are not used in the mode simulations because we found a large variation in optical constants as the material is reduced to nanoscale dimensions[3]. Similarly, the right panel of Fig. S2a shows the TE mode profiles of 30nm Sb_2Se_3 cladded SOI planarized waveguides with SLG. We use a cutback method to extract the on-waveguide optical constants of Sb_2Se_3 (See section S5 below) which are used in simulations. Since the refractive index change of Sb_2Se_3 is much smaller than that of GST, the shape of the optical mode remains roughly unchanged before and after phase transition. We calculated near zero loss in the simulation and a small change in the effective index $\Delta n_{eff} = 0.0017$. Such change is smaller than the recently reported value[4] but is consistent with our experimental extracted value of $\Delta n_{eff} \approx 0.0011$. We attribute the small discrepancy between the simulation and experiment to the fabrication variations and the slight reduction of material volume upon crystallization which we have neglected in simulation. Based on ellipsometry, we found ~11% reduction in Sb_2Se_3 thickness upon crystallization. Despite having smaller index change, the Sb_2Se_3 used in our work exhibits almost three times lower absorption loss in crystalline state (0.006 ± 0.002 dB/μm) compared to a recent work[4] and hence is highly desirable for phase shifter applications.

Next, we show that the PCMs have indeed reached the phase transition temperature by inputting the experimental conditions into the heat transfer model in COMSOL Multiphysics. The top panel of Fig. S2b shows that when we specify a current of 2.78mA (measured in experiments) and 400ns pulse width, the GST temperature reaches $\sim 700^oC$, $\sim 100^oC$ above the melting temperature of GST. The short trailing edge of 8ns ensures the melt-quench of the GST into the amorphous state. Similarly, by injecting 1.79mA (measured in experiments) into the SLG heater with a pulse width of 100μs, the GST is heated to $\sim 400^oC$. The 120μs long

trailing edge ensures the slow cooling of GST so that it settles into the crystalline state. The experimentally extracted SLG sheet resistance of 551±91 Ω/sq (see section S3 below) is used in the simulations.

Fig. S2c shows the temperature distribution in the cross-section of the device at the end of amorphization pule (t=400ns, top panel) and crystallization pulse (t=100μs, bottom panel). It can be seen from the heat distribution that the SLG heater exhibits an improved heating efficiency due to a two-fold effect. First, the SLG only has an atomically thin heating volume which significantly reduces the energy wastage, compared to a doped Si heater which has a gigantic heating volume coming from the 220nm thickness[2]. Secondly, the SLG and PCM are surrounded by ALD Al_2O_3 encapsulation top and bottom, which creates a large thermal boundary resistance between the SLG and the silicon slab below. This considerably reduces the heat dissipation into the silicon slab. Such phenomenon is clearly visible in the temperature distribution (Fig. S2c) where the heat is shown to be mainly confined in the SLG/PCM/Al_2O_3 thin film stack while the temperature of the silicon slab remains to be low.

S3. SLG sheet resistance and estimation of the switching power

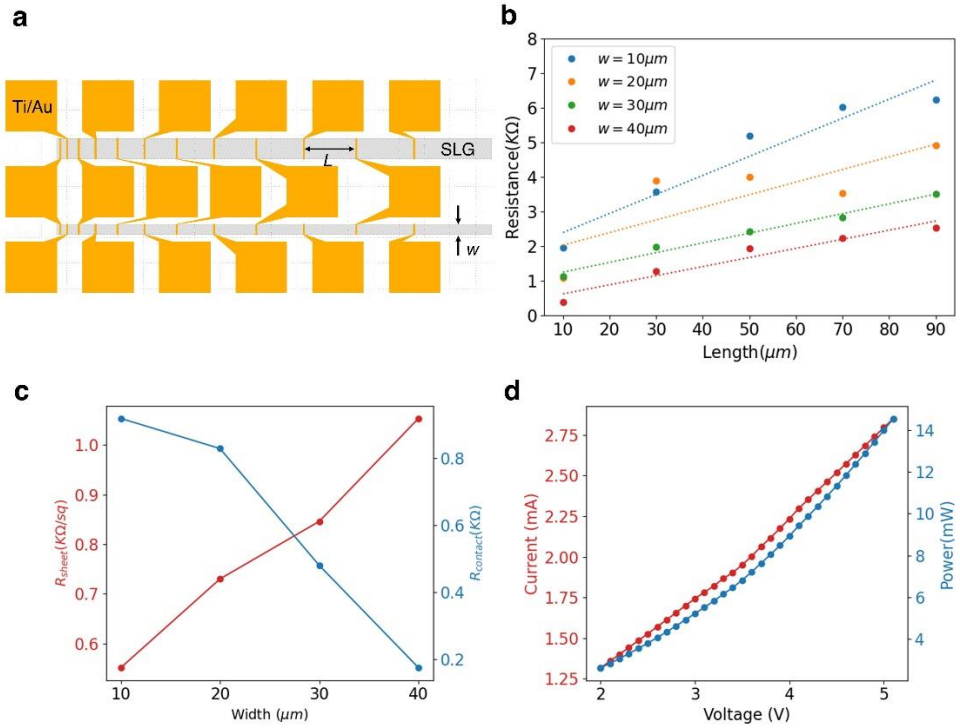

Figure S3: SLG sheet resistance and I-V curve. a Device schematic for characterizing the SLG sheet resistance. *W* is the SLG width while *L* is the SLG length. **b** Resistance of SLG of different widths against lengths. The resistance is measured at DC applied bias of 0.1mV. **c** The extracted sheet resistance and contact resistance of SLG against the width. **d** I-V curve of the SLG-GST device tested in the main text from 2V to 5.2V.

The sheet resistance of the SLG is extracted by an array of test devices next to the photonic switches with different lengths and widths of SLG connecting to metal contacts (Fig. S3a). The resistance is measured at 0.1mV DC bias and plotted against the SLG length (Fig. S3b). The sheet resistance is extracted by fitting the equation

$$R_{total} = 2R_{contact} + R_{sheet}\frac{L}{W}$$

to the experimental data. We extract the lowest sheet resistance $R_{sheet} = 551 \pm 91\Omega/sq$ at 10μm width and a contact resistance of $R_{contact} = 919 \pm 261\Omega$, as shown in Fig S3c. Ideally speaking, the SLG sheet resistance should not depend on the width, but in reality, we found

they are positively correlated. This is because the larger the SLG area, the more it is prone to defects such as pores and wrinkles, which means to obtain a low R_{sheet} it is essential to reduce the graphene area between the electrodes. To further reduce the SLG sheet resistance, hBN encapsulated SLG can be transferred mechanically, enabling high mobility charge transport[5]. On the other hand, Fig. S3c also shows that a large contact width between the SLG and the metals is required to reduce the $R_{contact}$. 1D edge contacts can be made to obtain ultra-low contact resistance and hence reduces the power loss in the contacts[6]. The total resistance of 1961±542Ω matches very well with the total resistance ~2000Ω that we measured from the SLG-PCM photonic switches.

To extract the programming energy per bit we measured the I-V curve of the devices to determine the power consumption. Fig. S3d shows the I-V curve from 2V to 5.2V of the ~5μm wide SLG heater that is used to switch the GST on SOI in the main text. The power is calculated to be 13.9mW (amorphization) and 5.37mW (crystallization), which gives the total energy per bit of 5.55nJ (400ns pulse width, amorphization) and 860.71nJ (100μs pulse width, 120μs trailing edge, crystallization). Although crystallization occurs at lower power than amorphization, it consumes higher energy as the pulse width and trailing edge are longer. The programming energy density can then be estimated by dividing the energy by the PCM volume. The GST volume is calculated to be 23nm×4730nm×400 nm, where the area is measured by SEM and thickness is measured by ellispometer. This yields an energy density of ~127.6aJ/nm^3 (amorphization) and ~19.78fJ/nm^3 (crystallization). However, a significant amount of power is lost in the contact resistance and does not contribute to heating the PCM. We now use the R_{sheet} extracted above to estimate the energy consumed solely in the heater region. The power consumed by the SLG heater region can be expressed as

$$P_{SLG} = I^2 R_{sheet} \frac{L}{W}$$

I is the measured current from the I-V curve (2.78mA at 5V for GST), *L* is the heater length which is measured to be 1.1μm, and *W* is the heater width which is measured to be 4.93μm. The programming energy consumed by the SLG heater alone is therefore 0.380±0.062 nJ (amorphization) and 63.3±10.3 nJ (crystallization). The programming energy density is 8.74±1.42 aJ/nm^3 (amorphization) 1.45±0.24 fJ/nm^3 (crystallization). This is a 20-fold reduction compared to the previous work using SLG heater, where the contact resistance was also subtracted[7], and 70-fold reduction compared to the most energy-efficient doped Si heater[2]. The programming energy for the SLG-Sb_2Se_3 phase shifter can be extracted in a similar fashion. The total switching energy for amorphization is ~9.25 nJ and the energy density is ~128.4 aJ/nm^3. The energy dissipated by the SLG heater alone (i.e., excluding the power loss at the contact resistance) is 0.57 ± 0.09 nJ, and the energy density is 7.90±1.28 aJ/nm^3. The total switching energy for crystallization is 1280 nJ and energy density is 26.67 fJ/nm^3. The energy consumed by the SLG heater alone is 78.7 ± 12.8 nJ and the energy density 1.09±0.18 fJ/nm^3. The table in section S8 summarizes the energy densities for both amorphization and crystallization which are compared to other works.

S4. Temporal trace of SLG-PCM photonic switch and phase shifter

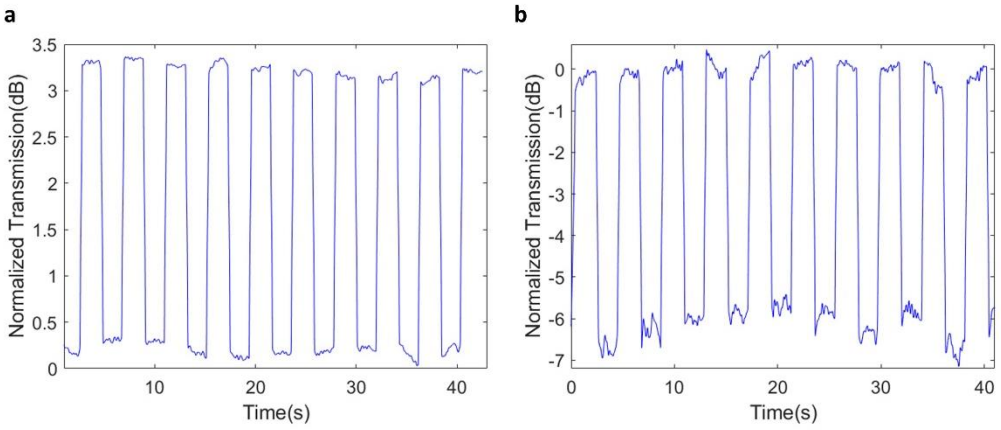

Figure S4: Temporal trace of SLG-PCM photonic switch and phase shifter. a Temporal trace of SLG-GST photonic switch for ten reversible switching events. The switching conditions are 3V, 100μs pulse width, 120μs trailing edge for SET and 5V, 400ns pulse width, 8ns trailing edge for RESET. **b** Temporal trace of SLG-Sb2Se3 phase shifter for ten reversible switching events. The switching conditions are 4V, 100μs pulse width, 120μs trailing edge for SET and 6.4V, 400ns pulse width, 8ns trailing edge for RESET. A two-second interval is used in **a** and **b** between consecutive switching events.

We continuously monitor the optical transmission over ten reversible switching events of the SLG-GST photonic switch (Fig. S4a) and the SLG-Sb_2Se_3 phase shifter in microrings (Fig. S4b) to show the dynamic response. The switching is deliberately paused for two seconds before the next excitation while the transmission is continuously measured. The transmission does not automatically fall back to the original state, indicating that the transition is indeed nonvolatile. The signal measured from the SLG-Sb_2Se_3 phase shifter is slightly noisier than the signal from the waveguide switch because the laser is parked near the resonance where the light intensity is very low. The up-shift and down-shift of the overall transmission background in Fig. S4b is caused by the resonance drifting from the temperature fluctuations.

S5. Cutback measurement of Sb_2Se_3 on microrings

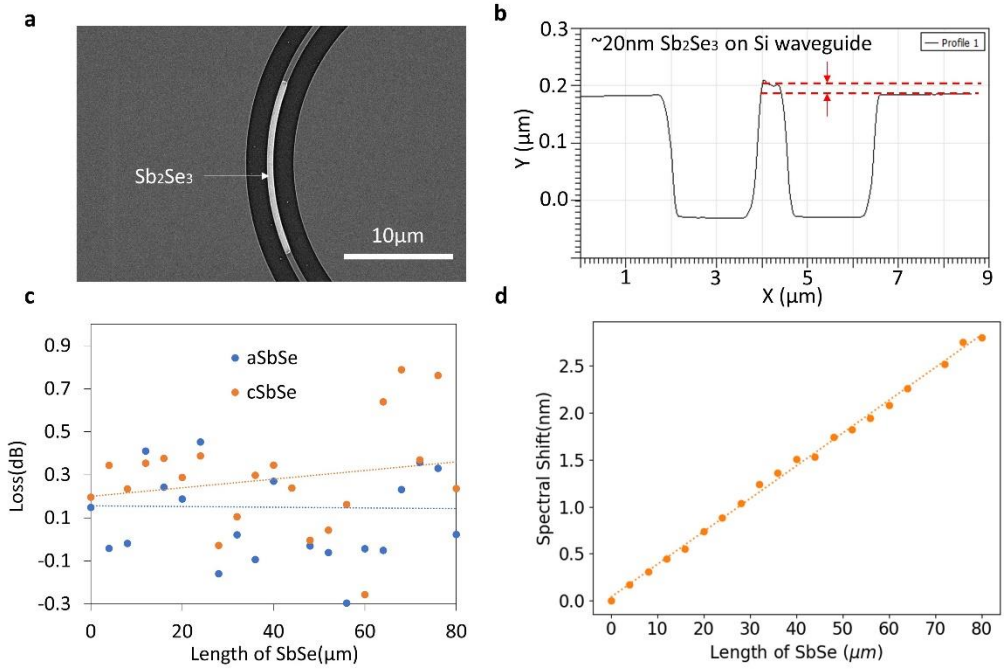

Figure S5: Extracting the insertion loss and effective index change of Sb_2Se_3 using microrings. a SEM showing the Sb_2Se_3 material is patterned on top the silicon microring resonators. **b** AFM measured cross-section of the waveguide with 20nm Sb_2Se_3 on top. **c** The extracted insertion loss of the Sb_2Se_3 in both the amorphous and crystalline states against the length. **d** The extracted spectral shift caused by the Sb_2Se_3 phase change against the length.

To evaluate the actual refractive index change and the loss of nanoscale Sb_2Se_3 on waveguides, we design a cutback measurement where the length of the Sb_2Se_3 cladded on 220nm fully etched silicon microrings is increased from 0µm to 80µm. Fig. S5a shows the SEM of a Sb_2Se_3 cladded microring where the PCM is only placed on top of the waveguide. Fig. S5b shows the waveguide cross-section measured by Atomic Force Microscope (AFM), indicating the thickness of the Sb_2Se_3 is 20nm. The loss and spectral shift with respect to the length of Sb_2Se_3 are plotted in Fig. S5c and S5d, respectively. A few data points show negative loss values due to fabrication variations such as resist residue and liftoff imperfections. By fitting the data, we extracted experimentally Δn_{eff} and Δk_{eff} as summarized in the table below using methods discussed in our previous works[1,3]

	Experiment
$\Delta\lambda(\mathrm{nm}/\mu\mathrm{m})$	0.035±0.000
Δn_{eff}	0.007±0.000
$\Delta\alpha(dB/\mu m)$	0.002±0.002
Δk_{eff}	$6 \times 10^{-5} \pm 6 \times 10^{-5}$

Finally, using the mode simulations, we estimate a $\Delta n \approx 0.008$ and a near zero extinction coefficient from the phase change of nanoscale Sb_2Se_3 on waveguides. These values are used to model the phase shift and insertion loss in our actual electrical switching devices, as discussed in section S2.

S6. Microrings spectra before and after endurance test

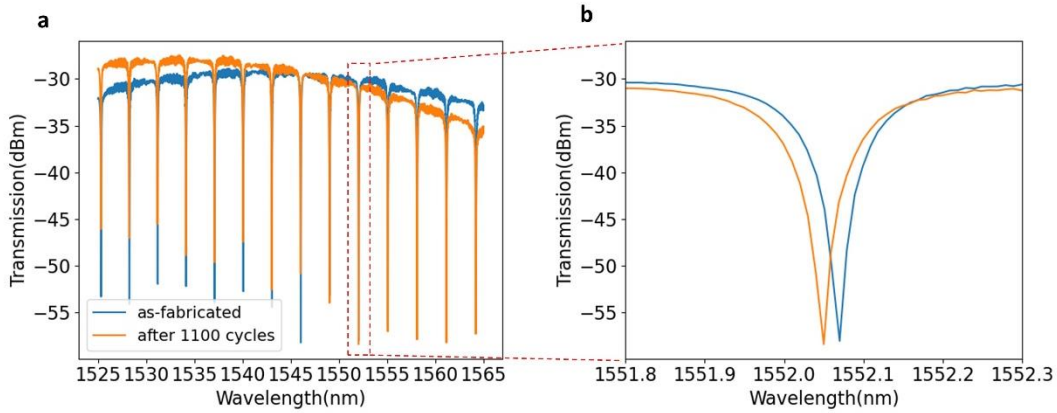

Figure S6: Spectra of the microring before and after the endurance test. a Spectrum of the as-fabricated microrings (blue) and the spectrum after 1,100 reversible switching cycles. **b** Zoomed-in of the resonance at 1552nm.

To show that the endurance test does not cause any damage to the devices, we plot the spectrum of the as-fabricated microring (i.e., microring that was just fabricated before any electrical switching; the devices are annealed at $200^{o}C$ for 10 mins to initialize the Sb_2Se_3 into the crystalline state) and the spectrum after 2200 switching events or 1,100 cycles. The two spectra overlap almost perfectly. Although microring resonators are very sensitive to any perturbations in the system, there is no sign of broadening of the resonance peak that suggests damage. The change in background spectrum is caused by the misalignment of the fibers with the grating couplers as the endurance test took over 2 hours to complete. Fig. S5b shows the resonance near 1552nm of the same spectrum. The blue shift of ~0.02nm suggests that the Sb_2Se_3 is in the amorphous state after the endurance tests, whereas the as-fabricated device was in the crystalline state.

S7. Performance degradation of SLG-PCM switches

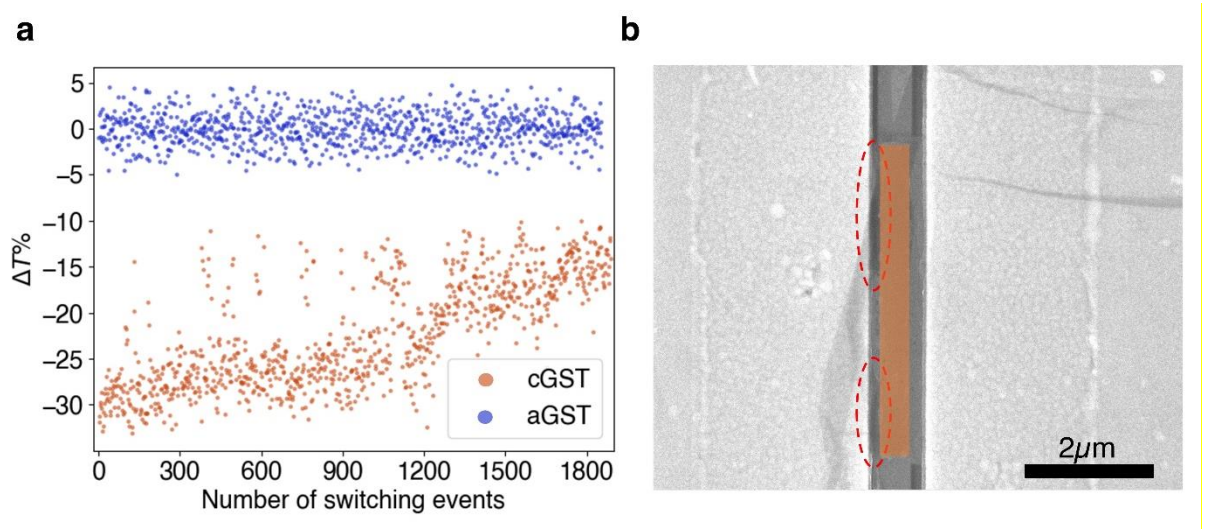

Figure S7: Performance degradation and failure mechanism of SLG-GST waveguide switch

a Degradation of transmission contrast over 1,800 switching events of the SLG-GST switch. The switching conditions are 3V, 100μs pulse width, 120μs trailing edge for SET and 5V, 400ns pulse width, 8ns trailing edge for RESET. **b** SEM showing the rupture of SLG in the red dashed circled regions. The GST strip is highlighted by the orange false color.

Fig. S7a shows the switching contrast degradation of the SLG-GST switch where the transmission contrast decreases from 30% to only 10% over 1,800 switching cycles. The contrast is defind as $\Delta T\% = \frac{T_{cry/am} - T_{am}^{ave}}{T_{am}^{ave}} \times 100$, where $T_{cry/am}$ is the transmission in crystalline/amorphous state, T_{am}^{ave} is the transmission in amorphous state filtered by a 2-point moving average. Fig. S7b shows the SEM of the same device after the endurance test. It can be clearly seen that the GST patch remains intact from the cycling but the graphene ruptures at left edge as indicated by the red dashed circles. As a result, the switchable area of the GST decreases. We believe the gradual breakdown of the graphene over thermal cycles is mainly caused by the oxidation. It is unlikely that such oxidation is caused by the atmospheric oxygen during the switching as the graphene is encapsulated by a thick layer of atomic layer deposited (ALD) Alumina. Rather, it may be resulted from the oxidizing residues collected over graphene

transfer and patterning, before it is encapsulated by the ALD Alumina. These oxidizing residues remain unreactive at room temperature but start to react with the graphene under high temperature, causing it to break.

S8. Raman spectrum of the graphene on fabricated devices

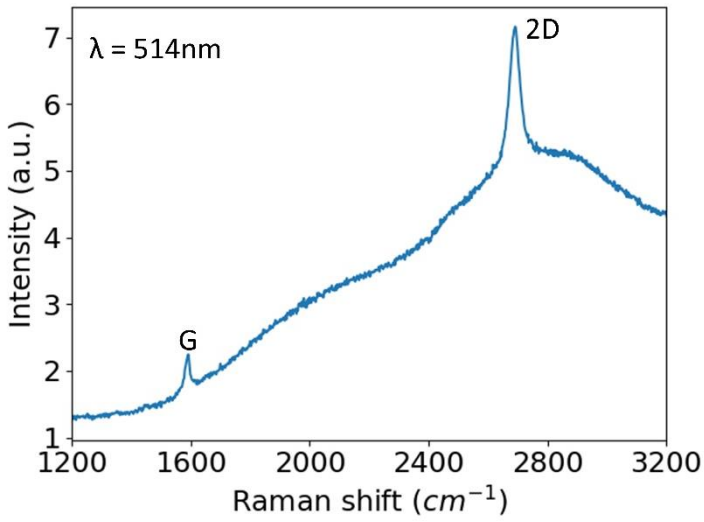

Figure S8: Raman spectrum of the graphene on the fabricated devices

Fig. S8 shows the Raman spectrum measured at the graphene region on the final fabricated devices. A 514nm wavelength laser is used at 1mW power. No defect-related peaks (D, D' or D+G) are observed, indicating that the subsequent fabrication after graphene transfer, including ALD, does not introduce structural defects into graphene. The absence of graphene oxide peak near 1300cm^{-1} shows that the ALD Alumina growth does not induce oxidation to the graphene.

S9. Transient reponse of SLG-PCM switches

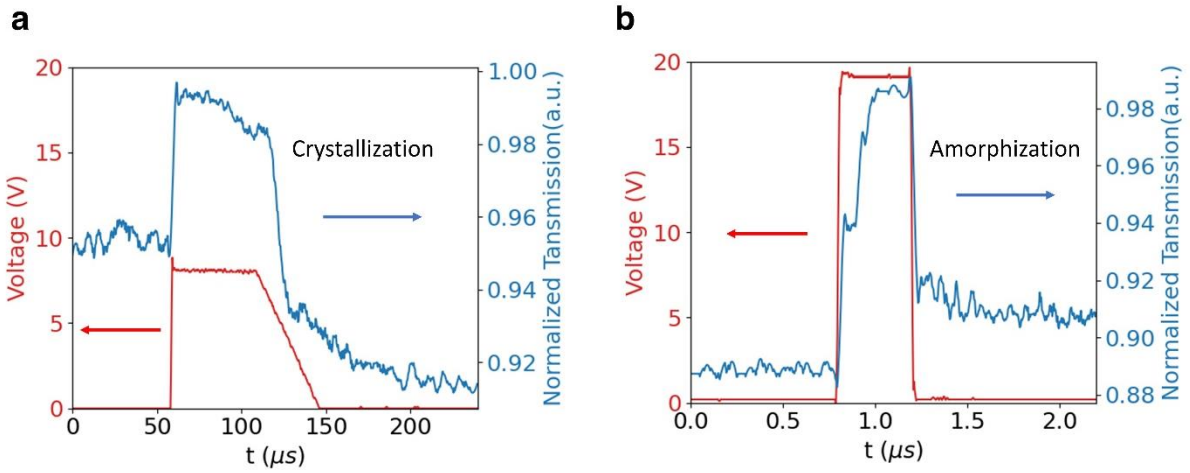

Figure S9: Real-time voltage of the applied electrical pulse and the corresponding change in transmission for (a) crystallization and (b) amorphization

We measured the response speed of SLG-Sb_2Se_3 waveguide switch using a 150MHz near IR fast photoreceiver (Thorlabs PDB450C). For crystallization, a 50μs wide pulse with 30μs trailing edge is applied to the heater at an amplitude of 8V. For amorphization, a 400ns wide pulse with 8ns trailing edge is applied to the heater at an amplitude of 19V. The relatively high voltage used is because of the high graphene resistance (~9KΩ) of the device under test. The small optical contrast is due to the small increase in optical absorption (~0.006dB/μm) in Sb_2Se_3. It can be seen that for crystallization, thermal relaxation takes longer time (~50 μs) due to the long pulse required. On the other hand, much faster response (~500 ns) is observed for amorphization thanks to the short excitation time (408 ns). The ultra-thin thermal mass of the graphene heater enables fast heat dissipation and hence short thermal relaxation, limited only by the duration of excitation.While it is hard to completely decouple the switching time due to material phase change from thermal relaxation, we think the reponse time is mainly limited by the thermal relaxation, instead of phase transition. This is because the change in dielectric constant caused by phase transition typically occurs at picosecond time scale[8], while heat diffusion normally requires hundreds of nanoseconds. We, however, would point out that for

most reconfigurable/ programmable photonics applications, switching speed is of low importance. The envisioned applications for PCM-photonics are programming a photonic circuit depending on the applications in hand. Due to the non-volatile nature of PCM, the static power consumption will be zero, and that is where we get the benefit of using PCMs. In such applications, it does not matter how fast we are programming the circuit, as the programming happens occasionally.

S10. Comparison to other nonvolatile electrically reconfigurable photonic platforms

We now compare our graphene-PCM hybrid platform to other electrical switching approaches in PCM-based photonics. Fig. S10 plots the number of switching cycles demonstrated against the programming energy density of recent works reporting electrical tuning of PCMs in photonics. We emphasize that the number of cycles demonstrated does not reflect the ultimate limit of PCM technologies since much higher cycle number[9] has been demonstrated in the electronic memory before. In fact, we anticipate increased number of cycles will be eventually realized in phase-change photonics as well. Our result shows the state-of-the-art in phase-change photonics and serves as a general guide to researchers when it comes to the choice of microheaters for phase-change photonics. The programming energy density is defined as the switching energy per unit volume of PCMs for complete phase transition, $\frac{E_{switch}}{V_{PCM}}$. The normalization with respect to PCM volume will ensure a fair comparison between different heater/switch geometries without considering the device architecture. Specifically, a microring and waveguide-based modulators will have vastly different switching energy due to the photon storage in the microring, but similar switching energy density. Here, we focus on low-loss conductors including doped silicon, TCOs, and graphene as they afford low insertion loss for integrated photonic applications. It can be seen that doped silicon[4,10] and PIN[2] heaters generally have remarkable endurance with the highest demonstrated cyclability of 500 cycles using a PIN heater[2]. However, they are all plagued by relatively high programming energy which lies between 600 and 800 aJ/nm^3, indicated in the grey region. The low energy efficiency is a result of large heating volume due to severe heat dissipation into silicon. For example, in order to change ~10-20 nm thick PCM, a 220 nm thick silicon waveguide has to be heated up to the PCM melting point, leading to significant power waste[11]. Lastly, such heaters cannot be used with materials that cannot be doped, such as Si_3N_4. On the other hand, TCO heaters have programming energies that are drastically different[12–14]. This is in contrast to the theoretical

calculation,[11] which predicts comparable energy efficiency between the silicon and ITO heaters. We attribute this to the substantial property variation between different growth conditions[15–17] of TCOs, whereas the growth and doping conditions of silicon is relatively standardized. Although high endurance (1,000 cycles) was shown using a fluorine-doped tin oxide (FTO) heater[14], the switching is not demonstrated in integrated photonics and the energy efficiency is very low. Meanwhile, ITO heaters are more widely explored for integrated photonics but suffer from endurance issues[3,12,13]. Finally, we compare our work to the recent demonstration of graphene heater for tuning $Ge_2Sb_2Se_4Te$ (GSST)[7] where the reversible switching is demonstrated, yet not in PICs. The endurance of GSST on graphene heaters has yet to reach the same level as previously demonstrated using metal heaters[18]. Introducing a graphene heater drastically reduces the total programming energy to 186 aJ/nm^3 in the previous work and reaches staggeringly low switching energy of 8.7 ± 1.4 aJ/nm^3 in our approach, when the power loss due to the contact resistance is subtracted. The extracted switching energy is very close to the simulated value[11] of 6.6 aJ/nm^3 and within one order of magnitude of the 1.2 aJ/nm^3 fundamental thermodynamic limit of GST phase change[9]. Such ultra-low programming energy density represents a 20-fold reduction in energy compared to the previous graphene heater[7] and a 70-fold reduction compared to the most energy-efficient doped silicon heater reported in literature[2]. The high energy efficiency is made possible primarily by the atomically thin heating volume of graphene which represents a ~650 times reduction in heating volume compared to the doped silicon for the same heater area. Secondly, the thermal boundary resistance between the graphene/Al_2O_3/Si thin film stack considerably limits thermal dissipation into the silicon underneath[11] (see also S2 for heat transfer simulations). On the other hand, the 20-times improvement in the energy efficiency of this work compared to the previous work on graphene can be attributed to a heater design specifically optimized for PICs. Instead of using a large graphene area ($\sim 100\mu m \times 10.5\mu m$), most of which does not contribute to the heating of PCM,

we reduce the extension regions down to only $\sim 0.3\mu m \times 5.2\mu m$. This confines graphene to the vicinity of the waveguide and PCMs (see Fig. 1 in main text), drastically minimizing the unnecessary heating and the power loss. In addition to energy efficiency, our work has also shown that graphene is a reliable heater with the highest cyclability of 1,000 cycles that has been demonstrated in electrically tunable phase-change PICs so far.

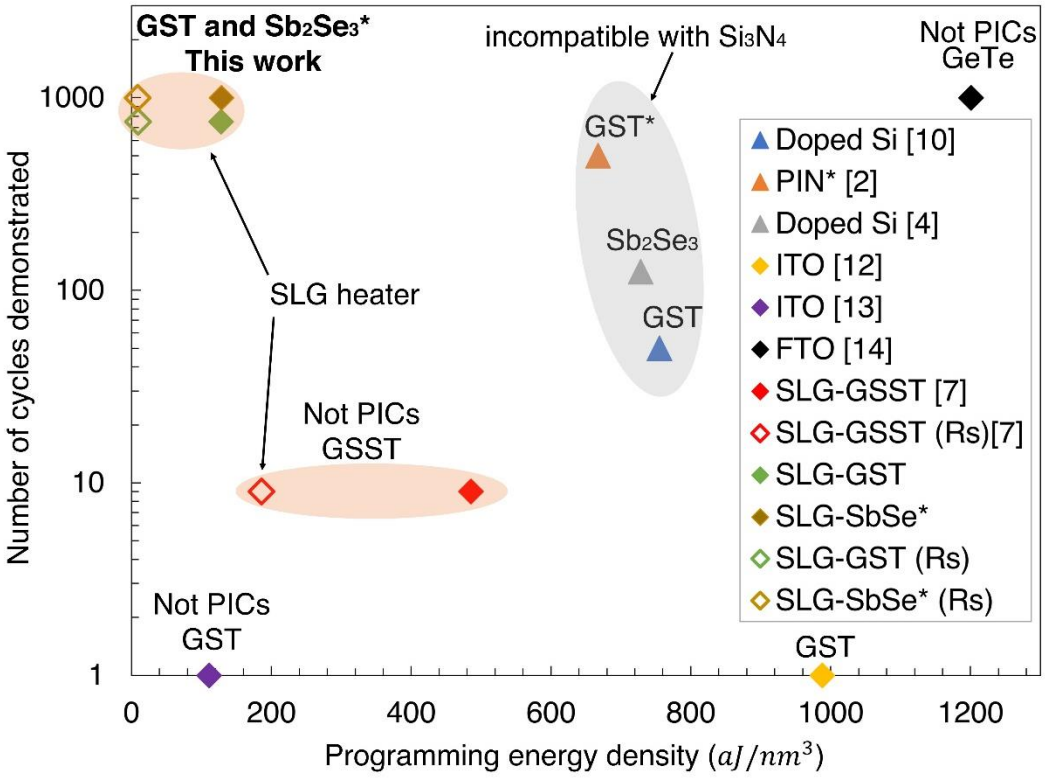

Figure S10: Comparison to other nonvolatile electrically reconfigurable photonic platforms

Comparison of number of cycles demonstrated versus the programming energy density for doped Si[4,10], PIN[2], TCOs[12–14], and graphene heaters[7]. The reference number is denoted inside the parenthesis. 'Not PICs' indicates that the reversible switching of PCM was not achieved on a PIC platform. The diamond markers indicate that the heaters are compatible with Si_3N_4. The no-fill diamond markers indicate the programming energy calculated by considering only the graphene sheet resistance, also denoted by 'R_s'. The grey shaded area includes only the doped Si heaters that are compatible with SOI only. The red shaded areas include only the graphene heaters. 'GST', 'GSST', and 'SbSe' in the legend denote $Ge_2Sb_2Te_5$, $Ge_2Sb_2Se_4Te$, and Sb_2Se_3 respectively. The * in the legend indicates that the numbers are quoted for microrings.

Table S1: Comparison to other nonvolatile electrically reconfigurable photonic platforms

		Amorphization				Crystallization						
Heater	PCM	Voltage (V)	Current (mA)	Power (mW)	Energy density (aJ/nm^3)	Voltage (V)	Current (mA)	Power (mW)	Energy density (aJ/nm^3)	Cyclability	Number of levels	compatibility with non-Si platforms
Doped Si[10]	GST	11.2	45	504	755	4.75	19	90.3	679	50	5	×
PIN[2]	GST	2.5	32	80	667	1	0.60	0.6	6500	500	2	×
Doped Si[4]	Sb_2Se_3	21	7.8	163.8	728	3.2	3	9.6	1.07E+05	125	9	×
ITO[12]	GST	10	20	200	988	6	12	72	3.56E+05	1	3	✓
ITO[13]	GST	9	22.5	202	111	3	0.2	22	5.67E+07	1	>2	✓
FTO[14]	GeTe	4	200	800	1200	3	150	450	2267	1,000	2	✓
Graphene[7]	GSST	7.5	2.99	22.4	485 (186)	6	2.39	14.3	4.95E+05 (1.84E+05)	9	4	✓
Graphene (this work)	GST and Sb_2Se_3	5	2.78	13.9	127.6 (8.74±1.42)	3	1.79	5.37	19779 (1454±236)	1,000	14	✓

The values in the parenthesis are the energy densities after subtracting the contact resistance. A graphical representation of part of the table is shown in the Figure S11 abvove.

S11. Comparison to optical switching of PCMs

Table S2: Comparison of the current work to optical switching PCMs

	Switching method	PCM	Amorphization energy density (aJ/nm^3)	Crystallization energy density (aJ/nm^3)	Insertion Loss (dB)	Cyclability	Scalability	Compatibility with transparent PCMs	PICs ?
Delaney et al.[19]	Optical (free space)	Sb_2Se_3	2435	1.65E8	0.5	500	poor	Yes in absorptive region	Yes
Delaney et al.[20]	Optical (free space)		354	8.84E8	NA	4,000	poor	Yes in absorptive region	No
Lawson et al.[21]	Optical (free space)		2613	6.11E8	NA	>1	poor	Yes in absorptive region	No
Rudé [22]	Optical (free space)	GST	69	260	2.5	>1	poor	Yes in absorptive region	Yes
Wu et al.[23]	Optical (on chip)		22	NA	0.46 and 0.75	>1	moderate	Yes in absorptive region	Yes
Stegmaier et al.[24]	Optical (on chip)		20	1889	4.3 and 5.1	1,000	moderate	Yes in absorptive region	Yes
This work	Electrical	GST and Sb_2Se_3	127.6 (8.74±1.42)	19779 (1454±236)	0.33	1,000	good	Yes	Yes

S12. Multilevel operation in waveguide switches and reproducibility

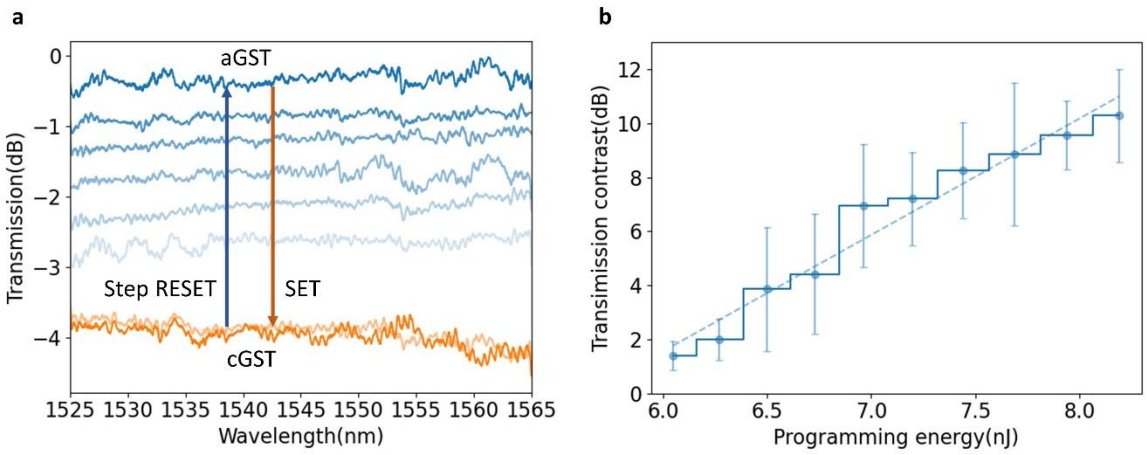

Figure S11: Multilevel operation in waveguide switches and reproducibility

a Multilevel operation of the SLG-GST waveguide switch through step amorphization. Seven distinct transmission levels are obtained by controlling the RESET pulse energy. The saturation of the blue color shows the level of amorphization. The light orange line indicates the initial crystalline state, while the saturated orange line indicates the as-switched crystalline state after the multilevel operation. The spectra are normalized with the spectrum of a bare waveguide. **b** Reproducibility of the multilevel operation evaluated by five iterations of SET and RESET cycles. Error bars indicate the standard deviation of transmission contrast for five iterations.

We show the multilevel operation of SLG-GST waveguide switch in Fig. S11a. Seven transmission levels can be attained by quasi-continuously tuning the RESET pulse energy from 5.71nJ to 6.49nJ. A SET pulse can be applied to return the RESET state into the initial crystalline state after the multilevel operation, as indicated by the light (initial) and saturated (SET) orange lines . It is well-known that multilevel operation of PCMs is inherently stochastic under electrical excitations[25]. In other words, the transmission levels attained by multi-stage crystallization/amorphization is generally not deterministic because the atomic configuration after each melt-quench process will never be the same. As a result, the crystalline domains formed by the SET pulses will have different sizes, shapes, and distribution for each SET-RESET cycle. In Fig. S11b, we assess the reproducibility of the ten-level operation in the SLG-

Sb_2Se_3 phase shifter by repeating the SET-RESET cycles for five iterations. Although the transmission levels are not deterministic, they all lie within the error bars and the mean transmission contrast across five iterations is positively correlated with the RESET pulse energy. While more transmission levels have been achieved using GST[26] by optical switching, this is usually limited by the signal-to-noise in experiment. In our measurements, the contrast between levels is around 0.5 dB which is hardly larger than the measured power fluctuation ± 0.2 dB. To relax the requirement for low noise, we either need to use larger GST volume or resonators to increase the transmission contrast. This is also why we achieved more transmission level in the Sb_2Se_3 graphene phase shifter due to the use of microrings.

References:

1. Zheng, J. *et al.* GST-on-silicon hybrid nanophotonic integrated circuits: a non-volatile quasi-continuously reprogrammable platform. *Opt. Mater. Express, OME* **8**, 1551–1561 (2018).
2. Zheng, J. *et al.* Nonvolatile Electrically Reconfigurable Integrated Photonic Switch Enabled by a Silicon PIN Diode Heater. *Advanced Materials* **32**, 2001218 (2020).
3. Fang, Z. *et al.* Non-Volatile Reconfigurable Integrated Photonics Enabled by Broadband Low-Loss Phase Change Material. *Advanced Optical Materials* **9**, 2002049 (2021).
4. Ríos, C. *et al.* Ultra-compact nonvolatile photonics based on electrically reprogrammable transparent phase change materials. (2021).
5. Dean, C. R. *et al.* Boron nitride substrates for high-quality graphene electronics. *Nature Nanotech* **5**, 722–726 (2010).
6. Wang, L. *et al.* One-Dimensional Electrical Contact to a Two-Dimensional Material. *Science* **342**, 614–617 (2013).
7. Ríos, C. *et al.* Multi-Level Electro-Thermal Switching of Optical Phase-Change Materials Using Graphene. *Advanced Photonics Research* **2**, 2000034 (2021).
8. Waldecker, L. *et al.* Time-domain separation of optical properties from structural transitions in resonantly bonded materials. *Nature Mater* **14**, 991–995 (2015).
9. Raoux, S., Xiong, F., Wuttig, M. & Pop, E. Phase change materials and phase change memory. *MRS Bull.* **39**, 703–710 (2014).
10. Zhang, H. *et al.* Miniature Multilevel Optical Memristive Switch Using Phase Change Material. *ACS Photonics* **6**, 2205–2212 (2019).
11. Zheng, J., Zhu, S., Xu, P., Dunham, S. & Majumdar, A. Modeling Electrical Switching of Nonvolatile Phase-Change Integrated Nanophotonic Structures with Graphene Heaters. *ACS Appl. Mater. Interfaces* **12**, 21827–21836 (2020).

12. Kato, K., Kuwahara, M., Kawashima, H., Tsuruoka, T. & Tsuda, H. Current-driven phase-change optical gate switch using indium–tin-oxide heater. *Appl. Phys. Express* **10**, 072201 (2017).
13. Taghinejad, H. *et al.* ITO-based microheaters for reversible multi-stage switching of phase-change materials: towards miniaturized beyond-binary reconfigurable integrated photonics. *Opt. Express, OE* **29**, 20449–20462 (2021).
14. Youngblood, N. *et al.* Reconfigurable Low-Emissivity Optical Coating Using Ultrathin Phase Change Materials. *ACS Photonics* **9**, 90–100 (2022).
15. Fallah, H. R., Ghasemi, M., Hassanzadeh, A. & Steki, H. The effect of deposition rate on electrical, optical and structural properties of tin-doped indium oxide (ITO) films on glass at low substrate temperature. *Physica B: Condensed Matter* **373**, 274–279 (2006).
16. Nisha, M., Anusha, S., Antony, A., Manoj, R. & Jayaraj, M. K. Effect of substrate temperature on the growth of ITO thin films. *Applied Surface Science* **252**, 1430–1435 (2005).
17. Zhu, B. L. *et al.* Structural, electrical, and optical properties of F-doped SnO or SnO2 films prepared by RF reactive magnetron sputtering at different substrate temperatures and O2 fluxes. *Journal of Alloys and Compounds* **719**, 429–437 (2017).
18. Zhang, Y. *et al.* Broadband transparent optical phase change materials for high-performance nonvolatile photonics. *Nature Communications* **10**, 4279 (2019).
19. Delaney, M. *et al.* Nonvolatile programmable silicon photonics using an ultralow-loss Sb2Se3 phase change material. *Science Advances* **7**, eabg3500 (2021).
20. Delaney, M., Zeimpekis, I., Lawson, D., Hewak, D. W. & Muskens, O. L. A New Family of Ultralow Loss Reversible Phase-Change Materials for Photonic Integrated Circuits: Sb2S3 and Sb2Se3. *Advanced Functional Materials* **30**, 2002447 (2020).
21. Lawson, D., Hewak, D. W., Muskens, O. L. & Zeimpekis, I. Time-resolved reversible

optical switching of the ultralow-loss phase change material Sb2Se3. *J. Opt.* (2022) doi:10.1088/2040-8986/ac5ece.

22. Rudé, M. *et al.* Optical switching at 1.55 μm in silicon racetrack resonators using phase change materials. *Appl. Phys. Lett.* **103**, 141119 (2013).
23. Wu, C. *et al.* Low-Loss Integrated Photonic Switch Using Subwavelength Patterned Phase Change Material. *ACS Photonics* **6**, 87–92 (2019).
24. Stegmaier, M., Ríos, C., Bhaskaran, H., Wright, C. D. & Pernice, W. H. P. Nonvolatile All-Optical 1 × 2 Switch for Chipscale Photonic Networks. *Advanced Optical Materials* **5**, 1600346 (2017).
25. Tuma, T., Pantazi, A., Le Gallo, M., Sebastian, A. & Eleftheriou, E. Stochastic phase-change neurons. *Nature Nanotech* **11**, 693–699 (2016).
26. Li, X. *et al.* Fast and reliable storage using a 5 bit, nonvolatile photonic memory cell. *Optica, OPTICA* **6**, 1–6 (2019).